CORRELATION OF MECHANICAL PROPERTIES WITH MICROSTRUCTURES AND DEFORMATION MODES IN SELECTED HIGH STRENGTH ZIRCONIUM ALLOYS

A THESIS

Presented to

The Faculty of the Division of Graduate Studies

by

Calhoun Wilson Hendrix, Jr.

In Partial Fulfillment

of the Requirements for the Degree

Master of Science in Metallurgy

Georgia Institute of Technology

September, 1977

CORRELATION OF MECHANICAL PROPERTIES

WITH

MICROSTRUCTURES AND DEFORMATION MODES

IN SELECTED HIGH STRENGTH ZIRCONIUM ALLOYS

Approved:

Dr. Edgar A. Starke, Jr., Chairman

Dr. Saghana B. Chakrabortty

Dr. E. E. Underwood

Date approved by chairman 8/22/77

TABLE OF CONTENTS

ACKNOWLEDGEMENTS

The author would like to express his sincere appreciation to his thesis advisor, Dr. E.A. Starke, Jr. whose invaluable guidance made this work possible. He also thanks Dr. E.E. Underwood and Dr. S.B. Chakrabortty for their help in reviewing this work. The author also thanks Dr. Rick Gangloff for his help during this project.

The help and advice of Mr. John Rinker during all phases of this work is deeply appreciated. Mr. Ed Coyne has been of great assistance both during the actual work and during the final preparation. The author thanks Darlene Coyne for help in typing the final work. Mr. Charles Blackwood was of great service in preparing samples and in building the equipment needed for this work. The author also thanks his brother Bo for preparing the figures used in this work. He also thanks his fellow students for their help and advice. Finally, the author thanks his wife, Anne, for her support and assistance throughout this project.

The author would also like to thank the General Electric Foundation for financial support of this investigation.

LIST OF ILLUSTRATIONS

Figure | Page

Figure Page

LIST OF TABLES

SUMMARY

The microstructure and high temperature deformation behavior of two high strength zirconium alloys were investigated and compared. The alloys studied were Zr-3Sn-1Mo-1Nb (CX) and Zr-1.55Sn-1Mo-1.5Nb-1Al (CY) (in weight percent).

Two widely different microstructures were obtained for each alloy treatment. These were characterized using x-ray diffraction, optical metallography and transmission electron microscopy. The microstructural features were correlated with the strength and deformation modes of each condition. Relative strengths were obtained through diamond pyramid hardness testing and the deformation mode and high temperature strength measurements were carried out on specimens tested in uniaxial tension at 350°C.

CHAPTER I

INTRODUCTION

Zirconium and its various alloys have found extensive use in the nuclear industry for reactor core internals, i.e., pressure tubes and fuel cladding. The most widely used materials are zircaloys and Zr-2.5 wt.% Nb and their compositions and neutron capture cross sections[1] are shown in Table 1. Zr-2 and Zr-4 differ only in the amounts of minor constituents present, and Ni is removed from Zr-4 to reduce its susceptibility to hydrogen up-take. The alloys of Table 1 exhibit a combination of properties which are well suited for nuclear applications. All three materials have low capture cross sections for thermal neutrons and good creep and corrosion resistance in aqueous environment up to 350°C. A good combination of fabricability and high temperature strength can be obtained through optimization of thermo-mechanical treatments. These materials were not believed to be susceptible to radiation damage until very recently[2]. McDonald[1] has reviewed the alloys currently in use, their limitations, and prospects for future high strength alloy development.

Since the middle of the 1950's there has been some interest in zirconium alloy optimization and the various systems and thermo-mechanical treatments studies have been summarized by Williams[3].

Table 1. Mean Composition and Neutron Capture Cross Sections of Current Zirconium Alloys

Alloy	Sn	Cr	Fe	Ni	O	Nb	Neutron capture cross section
	(weight percent)						(cm^2/cm^3)
Zr-2	1.5	0.12	0.10	0.05	0.12	--	0.0101
Zr-4	1.5	0.22	0.10	.005	0.12	--	0.0102
Zr-2.5Nb	--	--	--	--	0.11	2.6	0.0106

Recently, the desire to develop a pressure tube which can operate satisfactorily at superheat temperatures (450°C-550°C) has stimulated interest in high strength zirconium alloy development. This operating condition increased plant efficiency[4]. In addition, high strength alloys allow reduction in tube wall thickness and thus improve fuel cycle efficiency by removing neutron absorbing material from the core. However, the alloys must maintain fuel integrity and satisfy current design codes[1]. Other considerations involve fuel cladding cracking, which is associated with the fuel pellet-zircaloy cladding interaction[2]. The exact mechanism of these failures are not clearly understood; however, current theories under consideration include stress corrosion cracking due to the hostile environment produced by fission products, e.g., iodine[5,6,7,8], and flow concentrations due to dislocation channeling[2]. Dislocation channeling is a process whereby glide dislocations remove radiation defects, forming cleared channels of defect-free crystal. Subsequent dislocation motion within the cleared channels becomes easier and concentrated deformation results[9].

Williams, et al.[4] have developed two high strength Zr-alloys which appear very attractive for superheat applications. The composition of these alloys, coded CX and CY, are given in Table 2. At present, no correlation has been made between microstructure, deformation modes, and mechanical properties of these materials and this study was undertaken to accomplish this task. In this regard the deformation modes prevalent in the CX and CY alloys for two widely different microstructures were studied. Related titanium

Table 2. Composition of CX and CY Alloys with Calculated Thermal Neutron Capture Cross Section

Alloy	Sn	Al	Mo	Nb	Neutron capture cross section
	(weight percent)				(cm^2/cm^3)
CX	3.18	--	1.05	1.10	0.00990
CY	2.05	1.02	1.57	1.07	0.01009

studies were relied upon to select suitable treatments for the desired microstructures and mechanical properties.

CHAPTER II

REVIEW OF THE LITERATURE

In reviewing the literature it was found that little basic work has been done in correlating microstructure and deformation modes in zirconium alloys, although much work has been done in the area of texture and its effect on subsequent deformation. Consequently, titanium alloy studies were also reviewed for insight into possible microstructure property correlations.

Related Titanium Studies

The increased use of titanium and its alloys in the aircraft industry has precipitated a great deal of work on all aspects of alloy development. A wide range of alloys displaying varied microstructures and properties has been obtained through alloy chemistry control and thermo-mechanical treatments. These alloys exhibit high strength to temperatures exceeding 400°C. The properties and metallurgy of titanium and zirconium are very similar, with the major difference being lower solubility of common alloying elements in the α phase of zirconium. Due to this difference much more of a particular solute must be added to titanium to produce a given strengthening effect. Otherwise the two materials are almost completely analogous. Both have a high temperature β(bcc) phase

which undergoes an allotropic transformation to the low temperature α (hcp) phase. The strengthening mechanisms associated with a particular additive are essentially the same. For instance, aluminum and tin are solid solution hardeners and stabilize the α (hcp) phase, while Mo, Nb, Si, and V are β (bcc) stabilizers and precipitation hardeners. A martensitic phase can be obtained in both titanium and zirconium systems by quenching suitable alloys from the α + β or β phase region[10,11], and significant strength increases can be obtained by this method. In certain titanium alloys an hcp transition phase, ω, can be obtained by appropriate quenching from the (α+β) or β phase region, or by annealing below the α+β/α transus. This phenomenon is also observed in zirconium alloys treated similarly[10,13].

Deformation Modes in Zirconium and Zircaloy

The crystal structures of zirconium at room temperature is hexagonal close packed (hcp). The crystallography and deformation modes for hcp materials have been reviewed by Partridge[14] and the deformation modes for pure zirconium have been discussed in several papers[10,14,15,16]. Slip occurs primarily on the prism $\{10\bar{1}0\}$ planes in $\langle 1\bar{2}10\rangle$ directions from room temperature to 400°C. $\{0002\}\langle 1\bar{2}10\rangle$ slip has been observed both at elevated temperatures and at room temperature for polycrystalline zirconium[17], and slip on $\{10\bar{1}1\}$ and $\{11\bar{2}\bar{1}\}$ in (c + a) directions has also been observed[18]. As is typical in hcp materials, twinning is an important deformation mode due to the limited number of available slip systems. In tension along the c axis, $\{10\bar{1}2\}\langle\bar{1}011\rangle$ and $\{1121\}\langle 1126\rangle$ twins are observed (Fig. 1). For c axis compression,

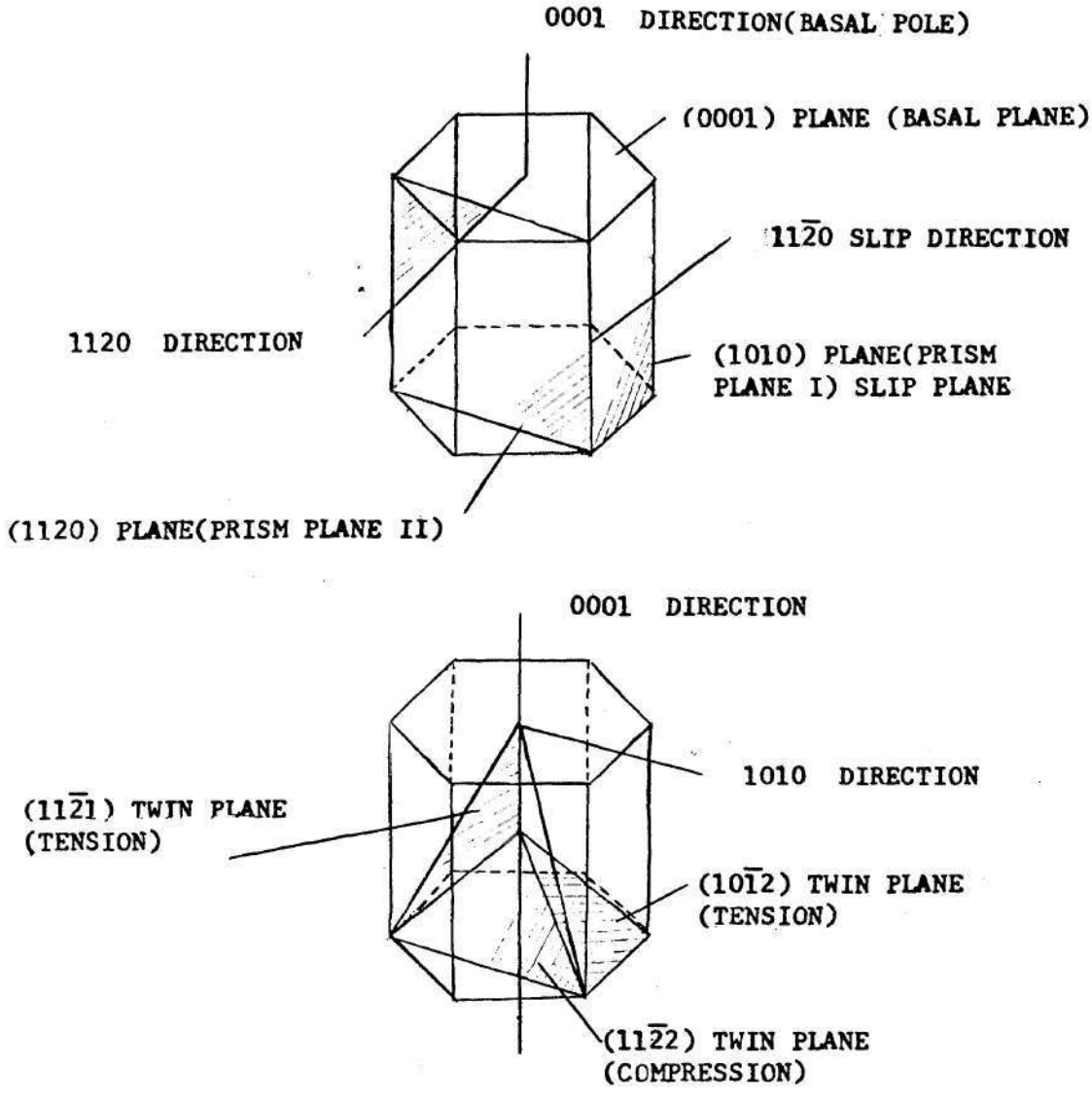

Figure 1. Deformation Systems and Crystallographic Planes and Directions in Zirconium.

$\{11\bar{2}2\}$ $\langle\bar{1}\bar{1}23\rangle$ type twinning occurs, and at elevated temperatures (>200°C) $\{10\bar{1}1\}$ $\langle\bar{1}012\rangle$ twins are observed[18]. $\{11\bar{2}3\}$ twins have been reported with no shear direction given[10].

The deformation modes in the zircaloys have not been subject to the definitive studies evident in pure zirconium. Katz[19] carried out the most extensive studies on deformation modes in Zircaloy-4. He found the primary slip system operating in cold rolled material to be $\{10\bar{1}0\}$ $\langle 1\bar{2}10\rangle$ and also observed $\{10\bar{1}1\}$ type slip in a few cases. Cross slip was very prevalent, even in the initial stages of cold work, and subgrains were formed. Dense tangled bands which tended to form cell structures in some areas were noted in heavily deformed materials[18]. (c + a) slip in thin bands close to $\{11\bar{2}4\}$ has been observed in plane strain compression of Zircaloy-4 along the <0001> direction[18]. Aqua and Owens[20] reported glide on at least two systems producing a characteristic cell structure in Zircaloy-4 cold rolled 2.5% reduction in thickness. The cell wall dislocations were primarily of the $\{10\bar{1}0\}$ type, indicating prismatic slip. It is known that twinning is an important deformation mode in Zircaloy, however, the twin planes have not been studied extensively. Twins of the $\{10\bar{1}1\}$ type have been identified after compression of Zircaloy-4 at temperatures greater than 300°C[18].

Texture

Because of the limited number of slip systems available, and the orientation relationship for slip and twinning in Zircaloy, a strong texture is developed during any fabrication process. On

subsequent heat treatment a strong annealing texture is formed which results in a highly anisotropic material (Table 3)[10]. The texture produced depends on the thermo-mechanical treatment given to the material, and since the greatest use of zircaloys has been in the tubular form, a great deal of effort has been placed on characterizing the texture developed during various tube forming processes. Douglas[10] has extensively reviewed the texture developed in various fabrication processes including tube forming.

Microstructure, Deformation Modes and Mechanical Property Correlation of Various Alloys

Oxygen is an α (hcp) phase stabilizer in zirconium and is present in trace amounts in almost all alloys. It has a profound effect on the mechanical properties, producing large strength increases when present in relatively small amounts. Bailey[21] has shown that this strength increase can be related to a change in the deformation mode. In relatively pure cyrstal bar zirconium he observed dislocation tangles along with loops and dipoles indicating that slip systems other than $\{10\bar{1}0\}$ were operating. Evidence was presented showing that basal slip was possible. In the commercial purity zirconium ($\sim$0.1 wt.%O_2+N_2) dislocations were comparatively straight and appeared to be more restricted to $\{10\bar{1}0\}$ planes.

Mo is a β (bcc) phase stabilizer in Zr. The strengthening effect of molybdenum additions to zirconium has been studied extensively, and covered in a review by Williams[3]. Domagola, et al.[22] studied zirconium base alloys containing 1.3, 3.3, 5.4 and 7.5 wt.% Mo, and found that the 1.3 wt.% Mo alloy had the best properties when

Table 3. Room-Temperature Anisotropy of Zircaloy-2

Specimen Orientation	Yield Strength (lbs/in^2)	
	Tension	Compression
RD	54,900	66,700
TD	58,300	62,700
ND	--	122,000

isothermally aged at approximately 600°-700°C. This treatment resulted in a coarse $\alpha + ZrMo_2$ structure. The higher concentrations of Mo yield extremely brittle materials possibly due to ω phase formation. Robinson, et al.[23] studied the hardening mechanism in a series of Zr-Mo alloys containing 5.5 wt.% Mo; 5 wt.% Mo, 2 wt.% Sn; 5 wt.% Nb, 2 wt.% Sn, and 2 wt.% Mo. The microstructural constituents were correlated with observed strengths. The alloys with high β stabilizer contents (Mo,Nb) were hardened by a transformation of the form:

$$\beta \rightarrow \omega + \beta \rightarrow \alpha + \beta_{enriched} \qquad (1)$$

where $\beta_{enriched}$ is a bcc phase rich in solute (i.e., Nb, Mo). The alloys with lower β stabilizer content are hardened by a reaction of the form:

$$\beta \rightarrow \alpha' \rightarrow \alpha + \beta_{enriched} \qquad (2)$$

where α' is martensitic α. In a program aimed at developing high strength zirconium, Williams, et al.[4] also studied effects of Mo additions to Zr. It was noted that due to the low solubility of Mo in Zr almost all of the alloying addition can be precipitated on aging, hence Mo is a very potent precipitation hardener. Due to neutron cross section considerations, the Mo addition was limited to 1 wt.%. Alloys with 1 wt.% Mo and 3 wt.% Sn were able to meet their development criteria. Little information concerning the

deformation mode change brought about by Mo additions was found in the literature although the stacking fault probability has been shown to increase with increasing Mo content[24] suggesting planar glide for Mo containing alloys.

Nb has proven to be an excellent strengthener for Zr as is evidenced by the extensive use of Zr-2.5 wt.% Nb in the nuclear industry. This is the strongest of the commonly used materials. Nb is a β phase stabilizer and a potent precipitation hardener forming the Nb rich β Nb phase ($\sim$ 85% Nb), however, little work has been done in actually characterizing microstructural changes with Nb additions and further correlating these with deformation mode changes. Aldridge and Cheadle[25] studied the effects of slow cooling from the $(\alpha+\beta)$ phase region and subsequent aging at 300°-500°C on the microstructure and strength of a Zr-2.5 wt.% Nb alloy. The microstructure formed consisted of α grains surrounded by a network of $\beta+\omega$ and gave excellent hardness and strength. Sabal[26] correlated the hardness increased in Zr-2.5 wt.% Nb to the formation of two distinct precipitates on aging at 500°C. Initially, a fine spherical precipitate is formed, which is later replaced by a needle-like precipitate. Williams, et al.[4] reported on the effects of Nb additions to Zr. Nb has a lesser strengthening effect than a comparable amount of Mo; however, it is used to reduce the neutron capture cross section of the resultant alloy while maintaining similar strengths. Cheadle and Ells[27] discussed the effects of Nb additions to Zr with respect to the onset of plastic instability in neutron irradiated materials. They found that Nb additions

increased the resistance of Zr to plastic instability and tended to decrease the size of defects formed during irradiation.

Of the two α stabilizers Al and Sn, Al has the greater strengthening effect. However, since it was noted that Al has a detrimental effect on corrosion resistance of Zr alloys in steam it has not been used as a strengthener to a great extent. The strengthening effects of Al additions to Zr have been reviewed by Williams[3]. Recently there has been some interest in the Zr-7.6 wt.% Al to 9 wt.% Al alloys which are based on the Zr_3Al ordered phase[28-31] This ordered phase is extremely stable, exhibits excellent strength at high temperatures, and possesses reasonable corrosion resistance. The effect of Al additions to Zr were also studied by Williams, et al.[4]. In addition to the excellent strengthening characteristics they noted that the Al additions tended to raise the density of basal faulting of the twinned martensitic α' in alloys quenched from near the β→α+β line. Al additions to Zr-Mo alloys also have a marked influence on the stability of the β (bcc) phase with respect to the formation of the ω phase[32,33]. For example, in Zr-3.0 wt.% Mo alloys the additions of 1 wt.% Al inhibits the formation of the isothermal ω during aging.

The α stabilizer and solution hardener Sn is the principal additive used in the two most common Zircaloys, Zircaloy 2 and 4. It has been studied extensively as a strengthener because it improves the resistance of Zr to corrosion in steam[3]. Sastry[34] has calculated the stacking fault energy for a series of Zr-Sn alloys containing 0, 0.7, 3 and 5 wt.% Sn. He noted a decrease in stacking

fault energy with increasing Sn content and proposed that the increased stability of attractive junctions is a strengthening factor for high temperature deformation in Zr-Sn alloys. Abson[35] studied the effects of Sn additions on substructure strengthening of the same alloys (0, 0.7, 3.5 wt.%) and noted minor changes in the dislocation structure, i.e., the cell walls became less distinct at higher Sn concentration. He also observed a decrease in subgrain size with increasing Sn content. Williams, et al.[4] has discussed the effects of Sn additions to various ternary and more complex alloys. Cheadle and Ells[27] noted that the addition of Sn to Zr decreased the amount of twinning observed in a neutron irradiated alloy.

It has been noted that the Zr-Cr-Fe alloys have a corrosion resistance in aqueous environment which is superior to the Zircaloys. For this reason there has been some interest in the strengthening mechanisms in this system[3]. Northwood[36] has correlated microstructures and properties in a Zr-1.15 wt.% Cr-0.1 wt% Fe alloy. He found that a β quenched and aged structure of martensitic α' with fine $ZrCr_2$ precipitates gave the best corrosion resistance, but showed some loss of ductility after irradiation. Substructural criteria for good corrosion resistance are given. The martensitic transformation in Zr-1.25 wt.% Cr-0.1 wt.% Fe was studied by Rumball[37] and the structures obtained from quenching from the β region at various rates were considered. A Zr-2 wt% Cr-0.16 wt% Fe quenched (~4500°C/sec) and aged at 300°C-500°C showed two distinct precipitates: a fine globular precipitate, and later in the aging process a fine needlelike one. This precipitation, which occured below the recrystallization temperature,

effectively pinned the grain boundaries and prevented grain growth during subsequent annealing[38,39].

The characteristics of Zircaloy-2 and 4, the most extensively used zirconium alloys in the nuclear industry, have been reviewed by McDonald[1]. The microstructures of the materials in the pre-irradiated condition have been studied to some degree, and because of the fabrication schedules for Zircaloys, much of the work has been concerned with the cold rolled state.

Kumar and Krishnan[40] noted that deformation due to cold rolling was very heterogeneous in Zircaloy-2 consisting of large dislocation chains or segmented braids. The deformation appeared to proceed on three glide systems. In highly deformed α' material, a cell structure was developed; however, it was not well defined. The microstructure of cold rolled Zircaloy-2 was also examined in conjunction with recrystallization studies[40]. The dislocation structure varied from areas of high dislocation density in the form of tangles to parallel bands of dense tangles. Little tendency to form cells was observed. The microstructure of Zircaloy-4 has been examined by Aqua and Owen[20], also in the cold rolled condition and was found to be very similar to that of cold rolled Zircaloy-2 discussed above. The dislocation structure was very inhomogeneous and cell structures were observed after small reductions (2.5%). A similar structure was not observed in Zircaloy-2 until after approximately 40% reduction. The cell walls in Zircaloy-4 were of a $\{10\bar{1}0\}$ $\langle 11\bar{2}0\rangle$ type. The maximum changes in microstructure and mechanical properties occured in the first 10% reduction, with much

slower changes on subsequent reduction.

The CX and CY were briefly mentioned in the Introduction. The mechanical properties of these alloys are superior to those of the Zircaloys and Zr-2.5 wt.% Nb while maintaining reasonable neutron capture cross-section and corrosion resistance[4,41,42,43]. The CY alloy has the same qualities with the exception of the corrosion resistance, which, due to presence of the Al, is lower than the Zircaloys or Zr-2.5 wt.% Nb. Table 4 gives the properties of CX, CY, Zircaloy 2 and Zr-2.5 wt.% Nb for comparison purposes. Microstructure and mechanical property correlations have been presented in some detail for alloy CX and to a lesser degree for the CY alloy. The best short term tensile properties were observed in samples water quenched and aged at approximately 500°C. This microstructure consisted of α' martensite with fine precipitates of β Nb or $ZrMo_2$, and tended to be brittle. However it was noted that the fine acicular α with a continuous network of transformed β obtained by air cooling from high in the $(\alpha+\beta)$ phase region gave properties which were as good, if not better, than the water quenched and aged material. Although the microstructure of these alloys has been characterized in some detail and correlated with the observed mechanical properties, no examination of deformation modes and comparisions of these to the Zircaloys has been published.

As can be seen from this literature review, the microstructures obtainable in zirconium alloys vary greatly with alloy additions and thermomechanical treatment. A limited amount of work has been done in correlating the microstructures with mechanical properties. However, an

Table 4. Tensile Properties of Zirconium Alloys

Alloy	Metallurgical Condition	Test Temp. °C	0.2% Yield Stress psiX10^3	UTS psiX10^3	% Uniform Elongation	% Total Elongation	% Reduction in Area
CX[1]	2h at 802°C slow cool	22	82	100	13	21	52
		302	49	61	12	20	64
CY[1]	as above	22	109	124	9.5	17	45
		302	72	90	9.0	15	52
CX[1]	air cooled from 927°C aged 6h at 627°C	22	101	112	9	18	50
		302	63	76	4	12	69
CX[1]	quenched from 927°C aged 6h at 527°C	22	175	190	1.5	4	19
		302	141	153	1.5	6	20
Zr-2.5 Wt% Nb[1]	Heat Treated	200	76L[4]	106L	--	--	45
			--	119T	--	--	46
		302	69L	86L	--	--	61
			95T	88T	--	--	50
Zr-2[2]	15-20% Cold drawn	300	45L	54L	--	26L	55L
			50T	52T	--	23T	54T
Zr-2[3]	Annealed 30 min. at 725°C	20	55L	--	--	--	--
			58T	--	--	--	--

1. After Ells & Cheadle[45]

2. After McDonald[1]

3. After Rittenhouse & Pickesimer[46]

4. L = Longitudal, T = Transverse

examination of the effects of a particular alloy additive or thermal treatments on the microstructure, and subsequently on the deformation modes, has not been attempted.

CHAPTER III

EXPERIMENTAL PROCEDURES

Material Preparation

The materials used in this project were prepared by General Electric Company using the consumable electrode method. Fifteen to twenty pound ingots of the CX and CY alloy were made using reactor grade zirconium. Each ingot was single melted in a vacuum arc furnace. The ends of each ingot were sawed off, approximately 100 mils was removed from the diameter by machining, and each ingot was sectioned axially. One half of each was processed to plate as per the following schedule: (a) heat in argon to 1040°C, forge to 0.5 in. thick plate, (b) anneal in argon at 1040°C for 30 minutes and water quench, and (c) heat to 730°C in argon hot roll to 0.180 in. in thickness. Each step was followed by a sand blast to remove the oxide layer formed during heating. Table 5 shows the spectrographic analysis of the alloy ingots.

The CX and CY alloy systems are very complex and not well understood. Figures 2 and 3 show the Zr rich corners of the Zr-Sn-Nb and Zr-Sn-Mo phase diagrams. The positions of the CX and CY alloys are noted on these diagrams. However, the effects of the other alloy additions on the $\beta/\alpha+\beta$ and the $\alpha+\beta/\alpha$ transus are not known. In order to choose a solutionizing temperature suitable for our studies it was necessary to more clearly define these transi. This was accomplished

Table 5. Spectrographic Analysis of CX and CY Alloy Ingots

Alloy	Sn	Nb	Mo	Al	O	N
		(weight percent, top/bottom)			(ppm)	(ppm)
CX	3.45/3.50	1.39/1.04	1.31/1.17	--	900/927	24/39
CY	1.54/1.40	1.58/1.57	1.12/1.04	1.05/1.0	840/921	27/33

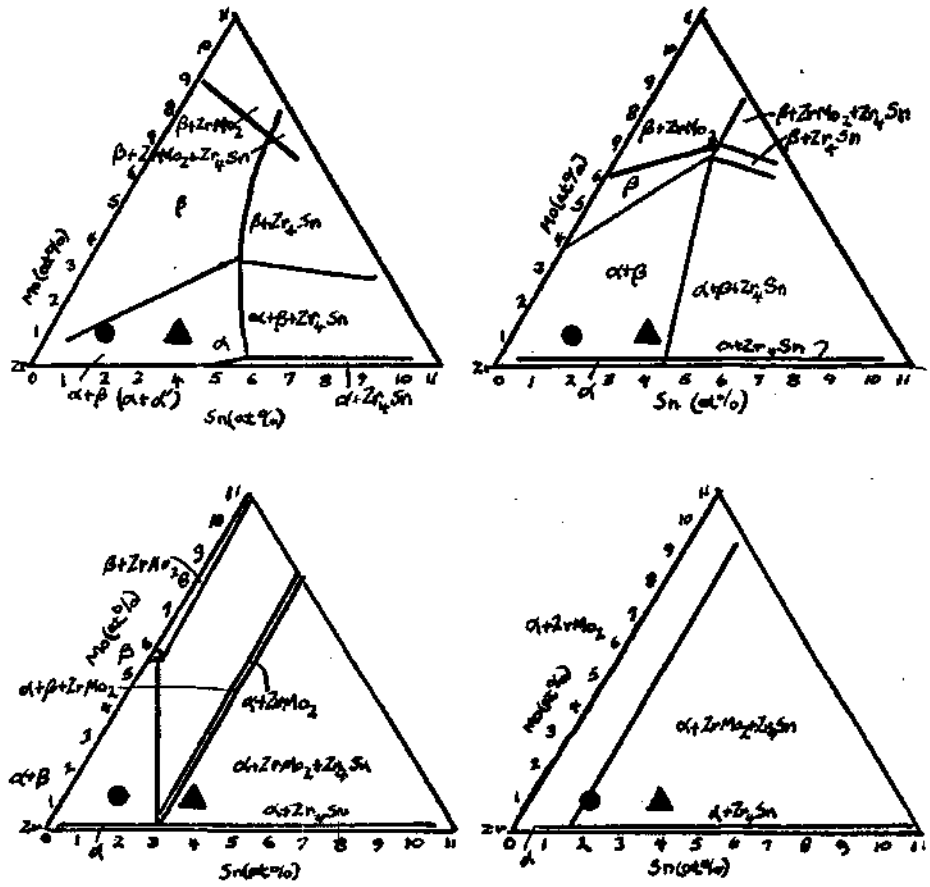

Figure 2. Zr-Sn-Mo Isotherms[12], CX Alloy Position Noted by ▲, CY by ● : (a) 900°C, (b) 800°C, (c) 700°C, and (d) 525°C.

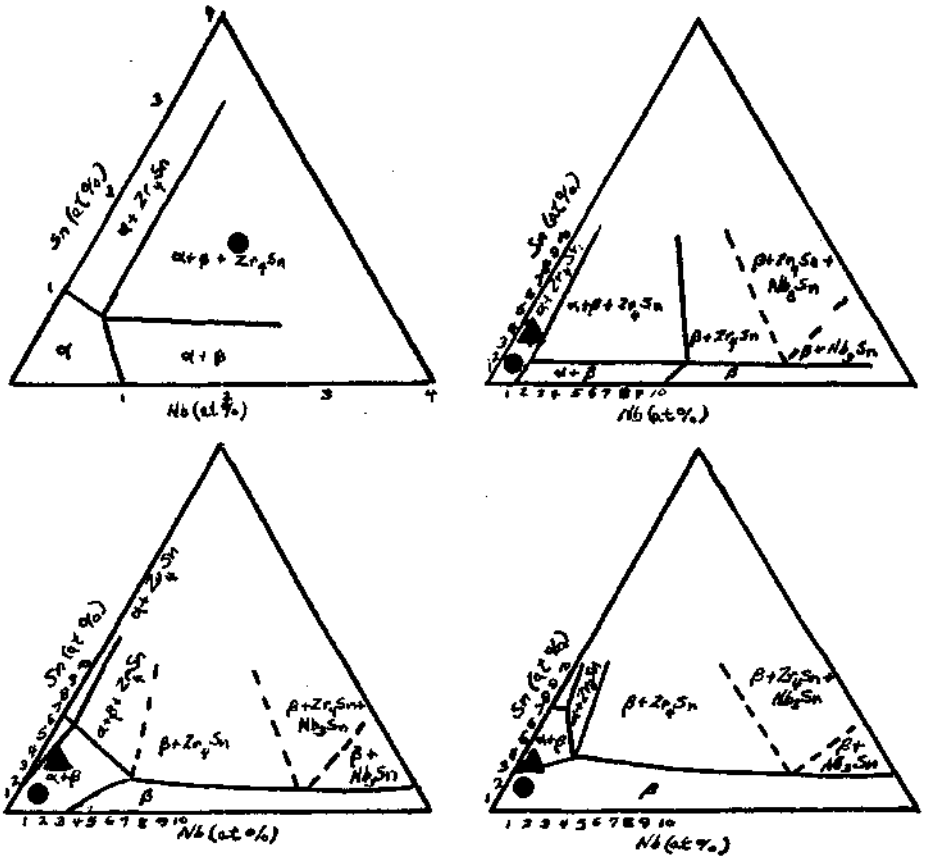

Figure 3. Zr-Sn-Nb Isotherms[12], CX Alloy Position Noted by ▲, and CY by ● : (a) 500°C, (b) 725°C, (c) 850°C, and (d) 940°C.

by dilatometry using a Orton Automatic Recording Dilatometer. The specimens were heated in argon to 1000°C and then furnace cooled. The cool-down curves were used since the possibility of the hot worked structure affecting the $\alpha/\alpha+\beta$ transus existed.

Two types of heat treatments were chosen to produce considerably different microstructures--furnace cooling and water quenching plus a one hour age at 450°C. Based on the dilatometry results three heat-treatment temperatures were chosen. Specimens were vacuum encapsulated in vycor tubing and solutionized one hour at 1000°C, 910°C or 800°C and either quenched in iced brine or furnace cooled at approximately 160°C/hr, through the $\alpha+\beta$ phase region. The oxide formed during quenching was removed by grinding and the specimens re-encapsulated in pyrex for aging at 450°C. In addition, a series of specimens were water quenched from temperatures ranging from 945°C to 800°C in order to study the effect of quench temperature on the strength and amount of $\beta+\omega$ or retained β formed. The microstructures were characterized by optical microscopy, x-ray diffraction and transmission electron microscopy. Specimens for optical microscopy were prepared using an etch attack-anodization technique described in Appendix 1. The volume fraction of the phases present was determined by the point count method[44] and the grain size by the Heyn method[45].

X-ray diffraction was used to identify the phases present in the alloy and to quantify the amount of retained β phase. The x-ray measurements were made using a modified G.E. XRD-6 diffractometer utilizing a doubly bent LiF primary beam monochromator and Ni-filtered Cu K_α radiation. The diffracted intensities were measured by continuous

scanning at 0.4^{o}/min using a xenon proportional counter with pulse height analysis. Integrated intensities for the quantitative determinations were obtained from the strip charts using a K+E compensating polar planimeter. The quantitative analysis method used was a modified direct comparison technique developed by Giamei and Freise[46]. This technique optimizes the normal direct comparison results by using all data available in the pattern including the diffraction peaks from each phase which were superimposed. A digital computer was employed to complete calculations involved in this method (Appendix 2).

A Siemens Texture Gonimeter was used to determine the (110) β and the (0002) α pole figures. The data were corrected for background and defocusing conditions and plotted with a CAL-COMP plotter. The pole figures were not normalized to random intensities but were plotted in arbitrary units.

Transmission electron microscopy (TEM) was used to finally characterize the alloy microstructures. TEM specimens were prepared by jet dimpling in a 20% perchloric acid in ethanol at -10^{o}C to -15^{o}C and 280V followed by polishing to perforation in 5% perchloric in ehtanol at temperatures ranging from -22^{o}C to -40^{o}C and 12V depending on the alloy and heat-treatment. The thinned foils were observed using a Siemens Elmscop IA operating at 125kV and a JEOL 100C at 100kV.

Mechanical properties were characterized using DPH hardness tests and tensile tests at 350^{o}C. Pin loaded type tensile specimens were used (Figure 4). The gauge sections of the specimens were polished to 0.5μ diamond prior to testing. The tensile tests were conducted

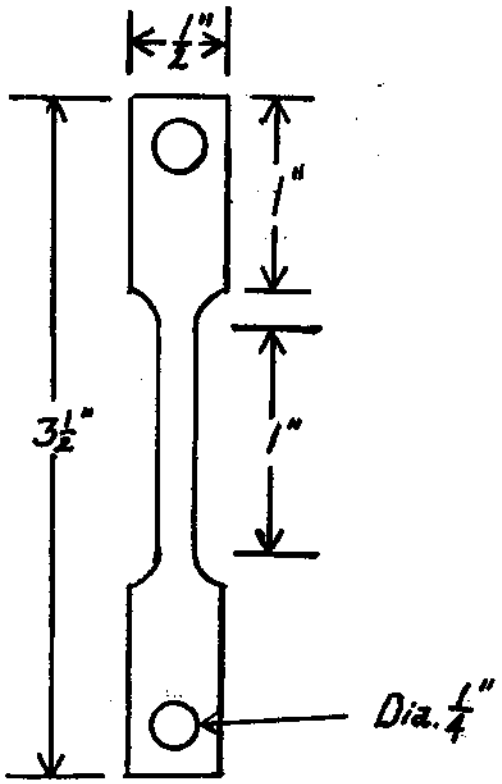

Figure 4. Tensile Specimens Used in 350°C Tests.

in dry argon at 350°C using the apparatus shown in Figure 5. An Instron tensile machine and a cross head speed of 0.1 in/min was used in all tests except those conducted on the 800°C solutionized materials. These materials were tested using an MTS machine at a cross head speed of 0.158 in/min. Gauge marks were used to evaluate strain at fracture on all specimens.

Deformation mode characterization was carried out using optical microscopy and TEM. Optical microscopy was performed on gauge sections of the tensile specimens to note any coarse deformation structures present. No mechanical or chemical polishing was done prior to these studies. TEM specimens were taken from the gauge section near the fracture surface and thin foils prepared as before. The foil surface was approximately parallel to the fracture surface, i.e., in most cases approximately 45° from tensile axis.

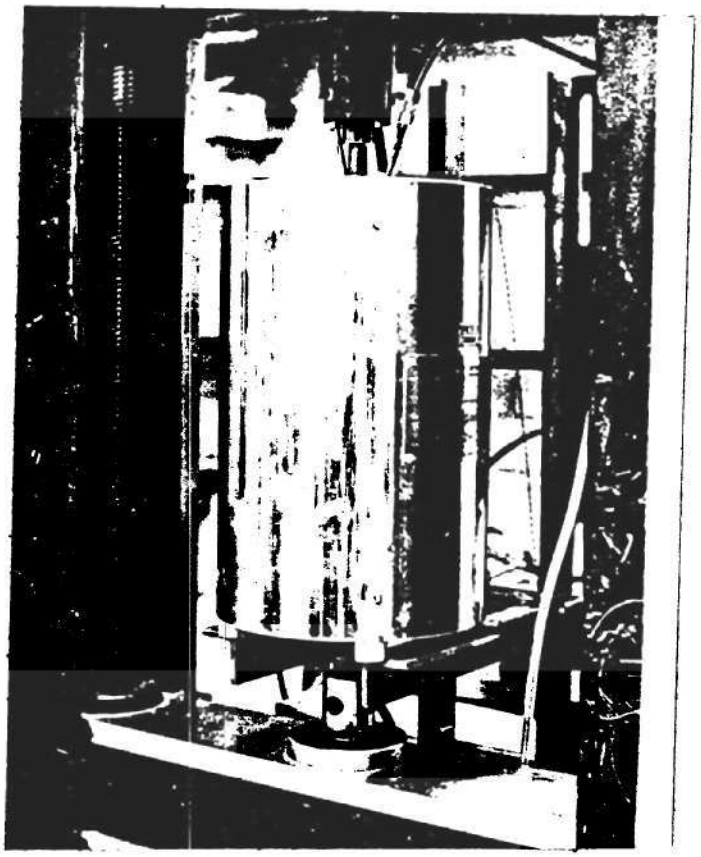

Figure 5. Picture of Apparatus.

CHAPTER IV

EXPERIMENTAL RESULTS

Heat Treatment

The results of dilatometry experiments for the CX and CY alloys indicate the $\beta \rightarrow \alpha+\beta$ reaction occurs between 950°C and 980°C and the $\beta+\alpha \rightarrow \alpha$ reaction between 680°C and 700°C for both alloys (Figure 6). These results are consistent with the phase diagrams of Figures 2 and 3 and with results for similar alloys[8] and suggest that minor additions of Mo, Nb, and Al have little or no effect on the transition temperatures.

Based on the dilatometry results, 1000°C, 910°C, and 800°C were chosen as solutionizing temperatures (shown in Figure 6). These temperatures provided the wide range of structures and strengths desired for this study. The structures obtained by water quenching from this series of temperatures ranged from 100% martensitic α' to 20% martensite in a matrix of primary α, allowing the relative strengthening effects of the martensite and primary α to be assessed. The materials that were water quenched from 800°C offered a less complicated structure with reasonable strength; however, contained significant amounts of $\beta+\omega$ which was considered undesirable due to the ω embrittlement and inherent complication of structure interpretation. Little or no $\beta+\omega$ was found in the materials water quenched from 1000°C and 910°C. Consequently, these solutionizing temperatures were chosen

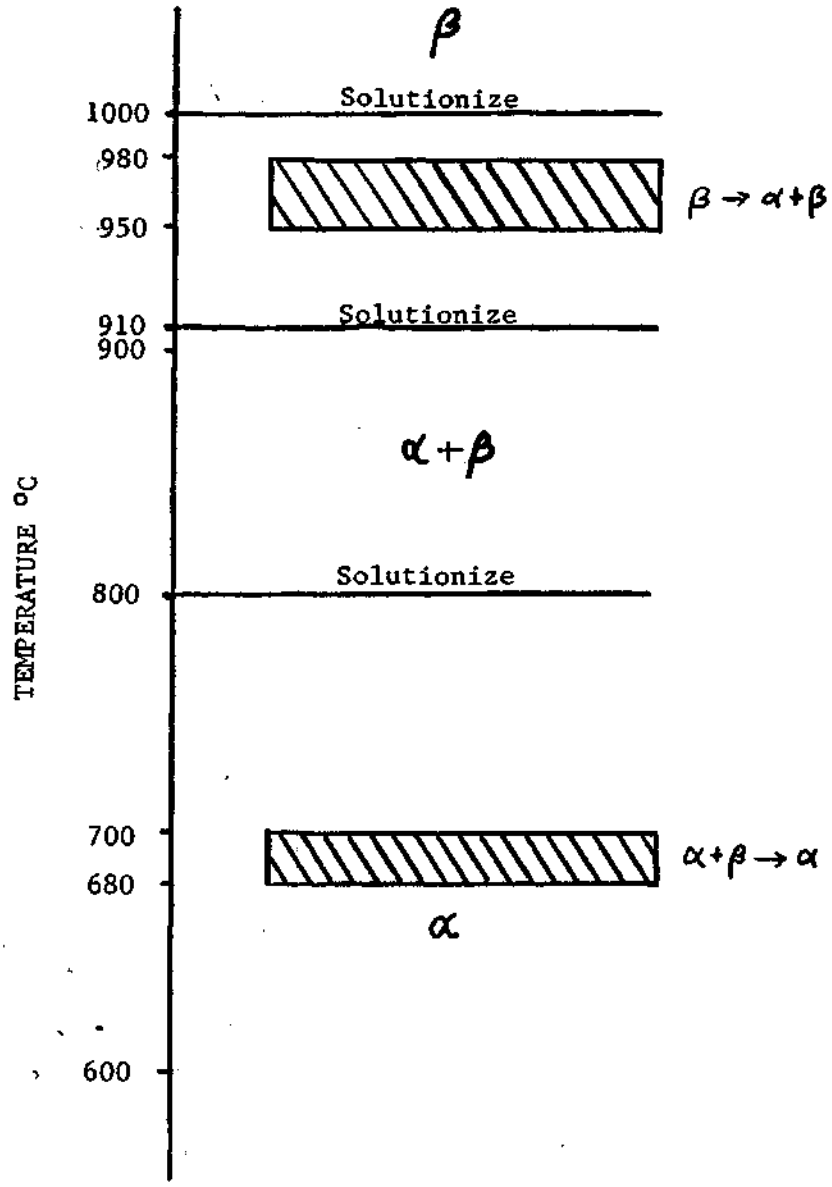

Figure 6. Phase Stability and Solutionizing Temperatures for the CX and CY Alloys.

for emphasis in the microstructural studies. In order to stabilize the water quenched structures against further changes during elevated temperature testing, all materials were aged 1 hour at 450°C. An added benefit of aging was the disappearance of the small amount of β+ω present in the 910°C water quenched material.

The materials which were furnace cooled from 910°C and 800°C exhibited an equilibrium structure and showed little difference due to the solutionizing temperatures. The small amount β or β+ω present was not considered a problem due to the overall simplicity of the structure.

Microstructure

Figure 7a shows a typical area in the CX alloy water quenched from 1000°C and aged 1 hr. at 450°C. Evidence of the large prior β grains can be seen. The width of these grains varied from 0.5 to 2.0 mm. The β grains tended to show the distinct contrast differences evidenced in Figure 7a. The structure within the prior β grains consisted of colonies of coarse martensitic α' plates in a matrix of finer plates (Figure 7b). In many cases the coarse plates extended the entire width of a prior β grain and had widths of 1-3μ (Table 6). The wide range of platelet sizes present in this heat treatment are evident in Figure 7b. The fine structure in these materials ranges from 0.5μ to less than 1000Å in width and as much as 10μ in length (Table 6). The martensite plates are seen to be heavily twinned, with twin size and spacing varying with α' platelet size. In the fine α' plates the twin size and spacing varied from 500 Å to 3000 Å (Table 6).

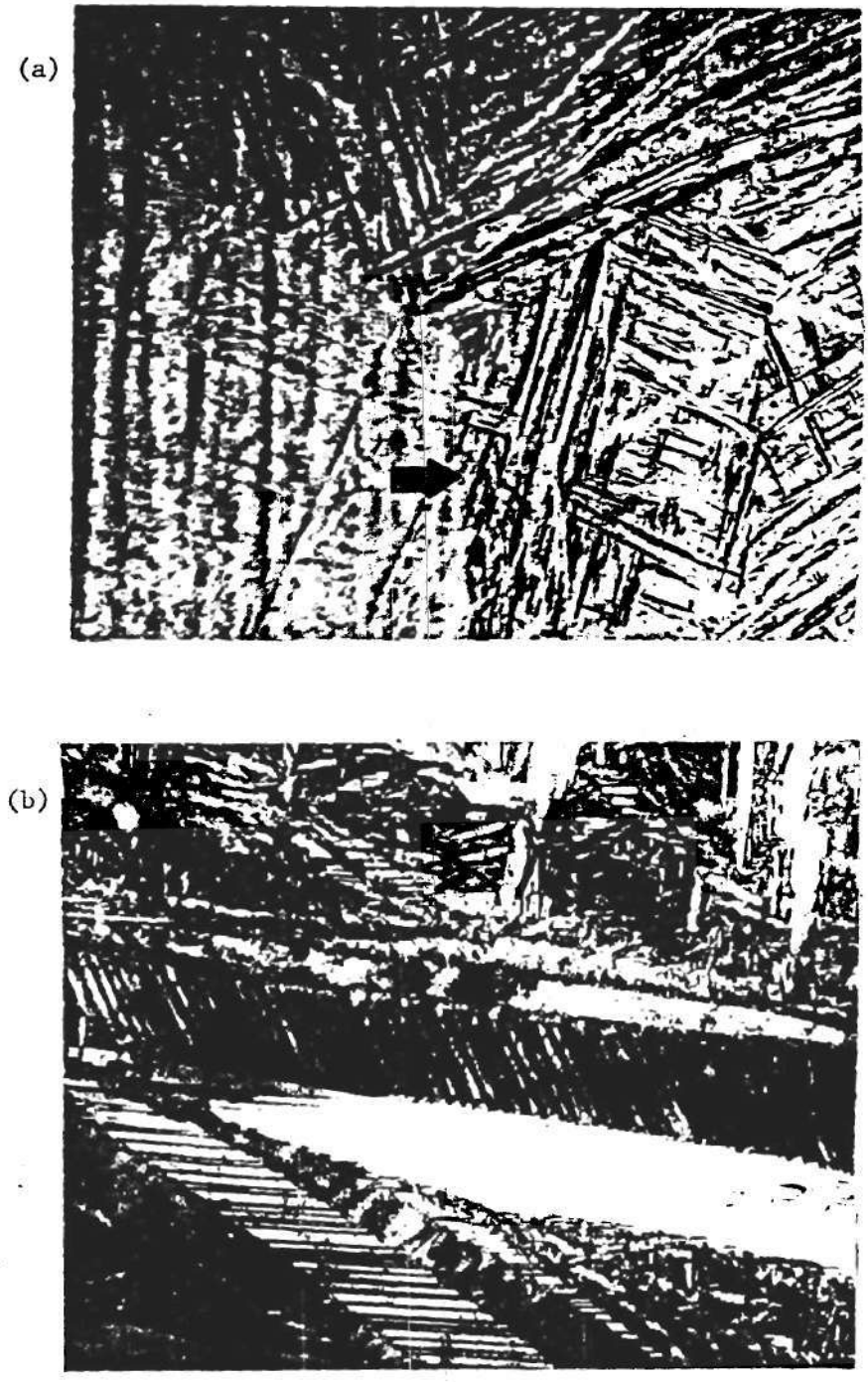

Figure 7. CX Alloy Water Quenched From 1000°C, Aged 1 Hr. at 450°C: (a) optical micrograph, unpolarized, 170X, showing a prior β grain boundary (arrowed), and (b) TEM of typical area showing large α' plates in matrix of very fine needles.

Table 6. CX Alloy Quantitative Metallography

Alloy and Heat Treatment	Volume Percent Isothermal α	Volume Percent Athermal α'	Isothermal α Grain Size	Athermal α' Grain Size	Athermal α' Twin Size	Athermal α' Twin Spacing
CX water quenched from 1000°C aged 1 h at 450°C	--	100	--	Coarse-2.0mm length x 1-3 μ width. Fine-5-10μ length x 0.5μ to 1000Å width.	Coarse-1000-5000Å Fine-500-3000Å	500-3000Å
CX water quenched from 910°C aged 1 h at 450°C	17	83	4.9μ	Coarse 5-20μ length, 1μ width. Fine-1μ length, 1000Å width.	500-2000Å	500-3000Å
CX water quenched from 800°C aged 1 h at 450°C	67	33	5.9μ	--	--	--
CX alloy furnace cooled from 910°C	23	77	3.7μ	--	--	--
CX alloy furnace cooled from 800°C	20	80	10μ	--	--	--

In the coarse α' plates twins were much larger ranging from 1000Å to 5000 Å in width; however, the range of twin spacings was similar to those in the fine plates (Table 6). In general, the smaller the α' platelets the finer and more closely spaced the twins. Figure 8 shows large numbers of homogeneously distributed precipitates. These are assumed to be Zr_4Sn or $ZrMo_2$ observed in similar systems and heat treatments[4,41]. The precipitates were too small and their volume fraction too low for detection by x-ray techniques. X-ray diffraction results for the 1000°C quenched and aged materials show these to be 100% α or α' martensite with no indication of β or ω. No systemic shift in d-spacing due to martensitic transformation product was noted.

The materials water quenched from 910°C and aged 1 hour at 450°C also showed prior β grains as did the 1000°C quenched and aged materials. The prior β grains were approximately the same size. Figure 9a shows this material to consist of small equiaxed grains in a continuous featureless matrix. Figure 9b shows the matrix to consist of very fine α' martensite plates. The equiaxed grains were identified by selected area diffraction as hcp α phase, and quantitative metallography showed the volume fraction to be 0.17 (Table 6). The grain size was 5μ (Table 6). The martensitic structure does not exhibit the large coarse martensite plates observed in the 1000°C quenched and aged materials. The martensite in the 910°C quenched and aged materials is, however, similar to the fine structure of the 1000°C quenched and aged materials. The smallest platelets resolvable had widths less than 1000 Å and lengths on the order of

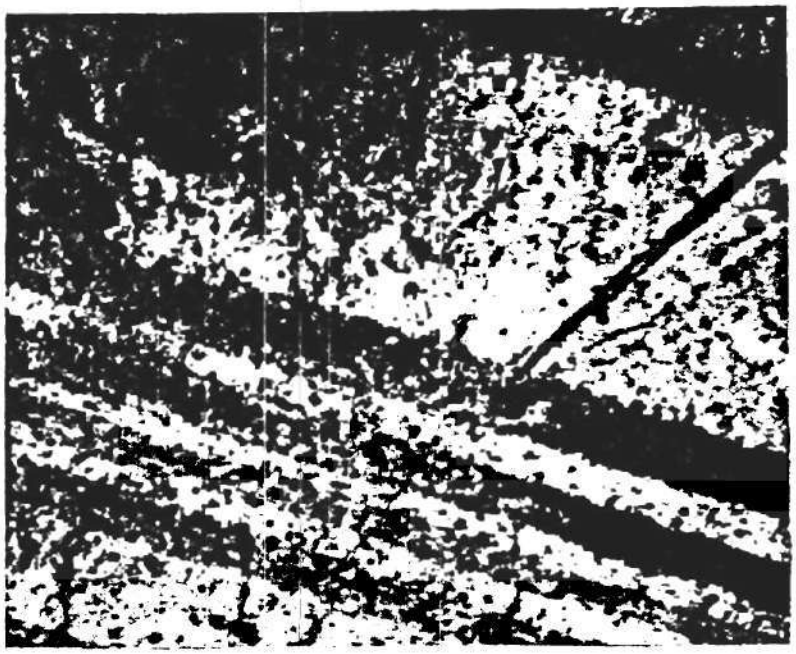

1000Å

Figure 8. CX Alloy Water Quenched from 1000°C, Aged 1 Hr. at 450°C. Fine Precipitates in Coarse α' Martensite Plates.

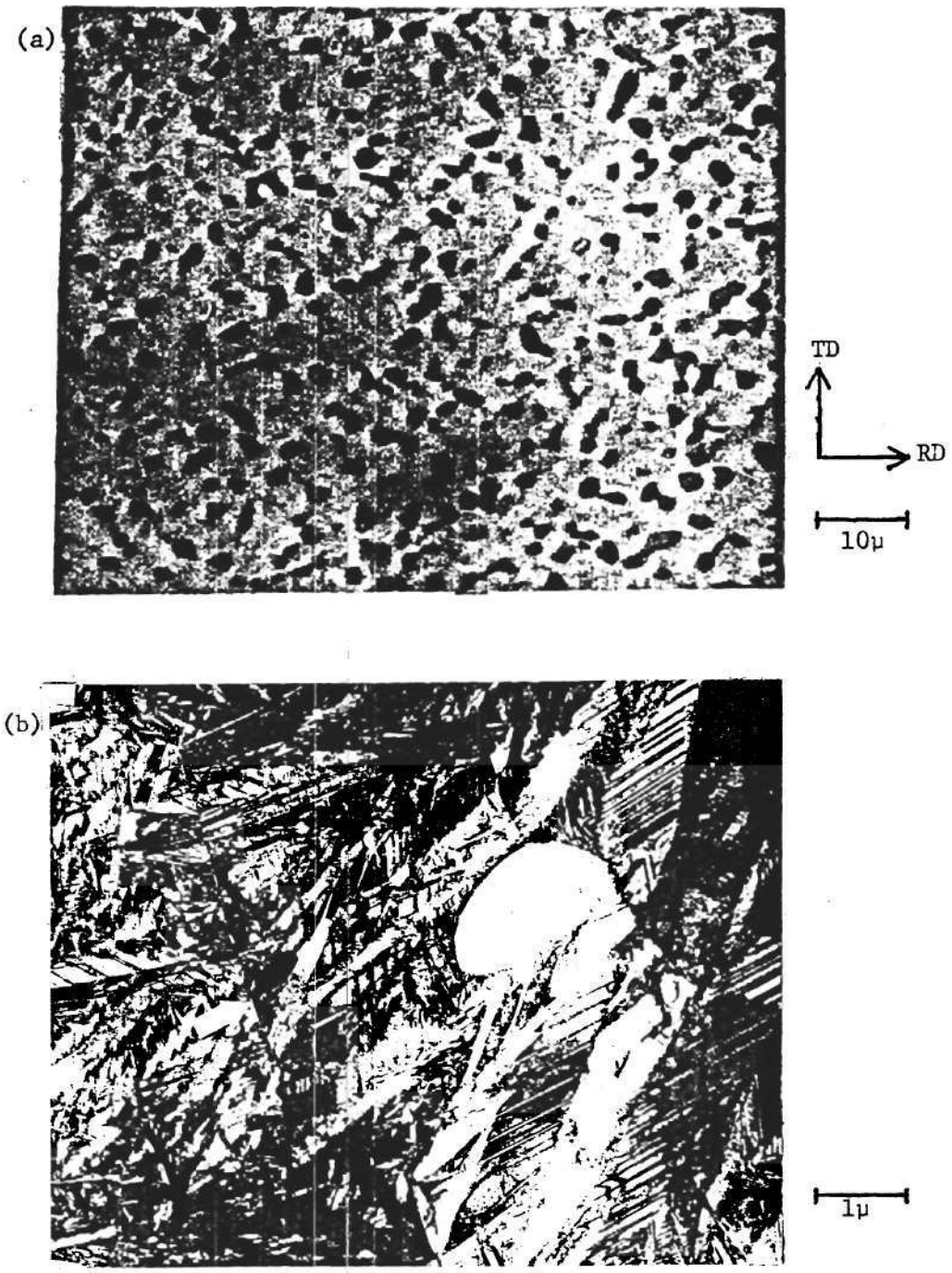

Figure 9. CX Alloy Water Quenched from 910°C, Aged 1 Hr. at 450°C:
(a) optical micrographs, unpolarized typical area,
(b) TEM, typical area, prior β grain boundary (arrowed).

several microns. It is felt that even finer unresolved plates are present. However, due to the complicated structure it was not possible to resolve these at higher magnifications. The largest plates in the 910°C quenched and aged materials were approximately 1μ in width and 5-20μ in length. These larger grains comprised a significant percentage of the structure. As in the 1000°C quenched and aged materials the twin size and spacing was related to the α' martensite plate size. Twin size and spacing are given in Table 6 with size varying from 500 Å to 2000 Å and spacing from 500 Å to several thousand angstroms. The primary α grains exhibited a large number of homogeneously distributed precipitates (Figure 10). These particles were somewhat larger than those noted in the α' plates of the 1000°C quenched and aged materials. Based on previous work[4,43], these precipitates are assumed to be Zr_4Sn or $ZrMo_2$.

Table 7 shows the observed d-spacings for the 910°C as-quenched and quenched and aged conditions. The calculated α Zr, β Zr, and ω d-spacings are also provided. Table 7 shows the 910°C water quenched materials to be primarily hcp α plus trace amounts of β Zr. After aging for one hour at 450°C, the trace amounts of β present had disappeared and a weak line appeared at d=1.30 Å. This line corresponds to the ω $(11\bar{2}2)$/β Zr (211) line and the β Nb (211) line.

The CX type alloy water quenched from 800°C and aged 1 hr. at 450°C, differed greatly from 1000°C and 910°C quenched and aged materials. Figure 11a shows this material to consist of primary α plates lying in mutually perpendicular directions. The primary α grains appear to be "pan-cake" shaped with a grain size of 7μ (Table 6).

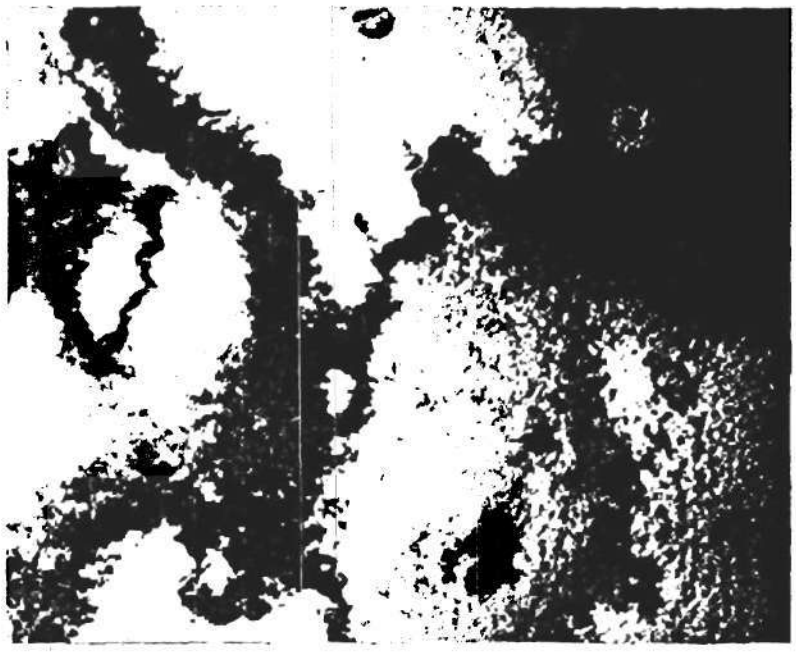

Figure 10. CX Alloy Water Quenched from 910°C, Aged 1 Hr. at 450°C, Showing Homogeneously Distributed Precipitates.

Table 7. Observed d-spacing for CX Alloy in the Water Quenched Condition

Observed d-spacing 910°C water quenched		Observed d-spacing 800°C as quenched		Observed d-spacing 910° quenched/aged		Observed d-spacing 800°C quenched/aged		α Zr		β Zr		ω	
d,Å	I,cps	d,Å	I,cps	d,Å	I,cps	d,Å	I,cps	d,Å	hkil	d,Å	hkl	d,Å	hkil
2.80	550	2.80	350	2.80	700	2.80	290	2.798	$10\bar{1}0$				
				2.79	325								
2.59	2175	2.58	1100	2.58	2700	2.58	350	2.573	0002				
2.53	300	2.52	1050			2.53	495			2.51	110	2.51	$10\bar{1}1,11\bar{2}0$
2.47	1850	2.46	1950	2.47	6600	2.47	3400	2.459	$10\bar{1}1$				
						1.97	20					1.95	$11\bar{2}1$
1.90	340	1.90	190	1.90	400	1.90	370	1.894	$10\bar{1}2$				
1.80	25	1.79	25			1.79	110			1.78	200	1.78	$20\bar{2}1$
1.63	80	1.62	25	1.63	30	1.62	50	1.616	$11\bar{2}0$			1.68	$30\bar{3}0$
												1.54	0002
1.47	400	1.47	223	1.47	370	1.47	330	1.463	$10\bar{1}3$				
		1.45	155							1.45	211	1.45	$21\bar{3}1$
1.40	60	1.40	40	1.40	100	1.40	40	1.399	$20\bar{2}0$				
1.37	123	1.37	105	1.37	160	1.37	70	1.368	$11\bar{2}2$				
		1.35	193	1.35	410	1.35	345	1.350	$20\bar{2}1$				
		1.33	18	1.30	50	1.33	30					1.31	$11\bar{2}2,30\bar{3}1$
1.29	68	1.29	43	1.29	170	1.29	75	1.287	0004				
		1.26	40			1.26	90			1.26	220	1.26	$22\bar{4}0$
1.24	30	1.23	38	1.23	170	1.23	100	1.229	$20\bar{2}2$				
1.17	40	1.17	40	1.17	40	1.17	60	1.168	$10\bar{1}4$			1.16	$22\bar{4}1$
		1.13	25			1.13	50			1.13	310	1.12	$31\bar{4}1$
1.09	73	1.09	90			1.09	195	1.084	$20\bar{2}3$				

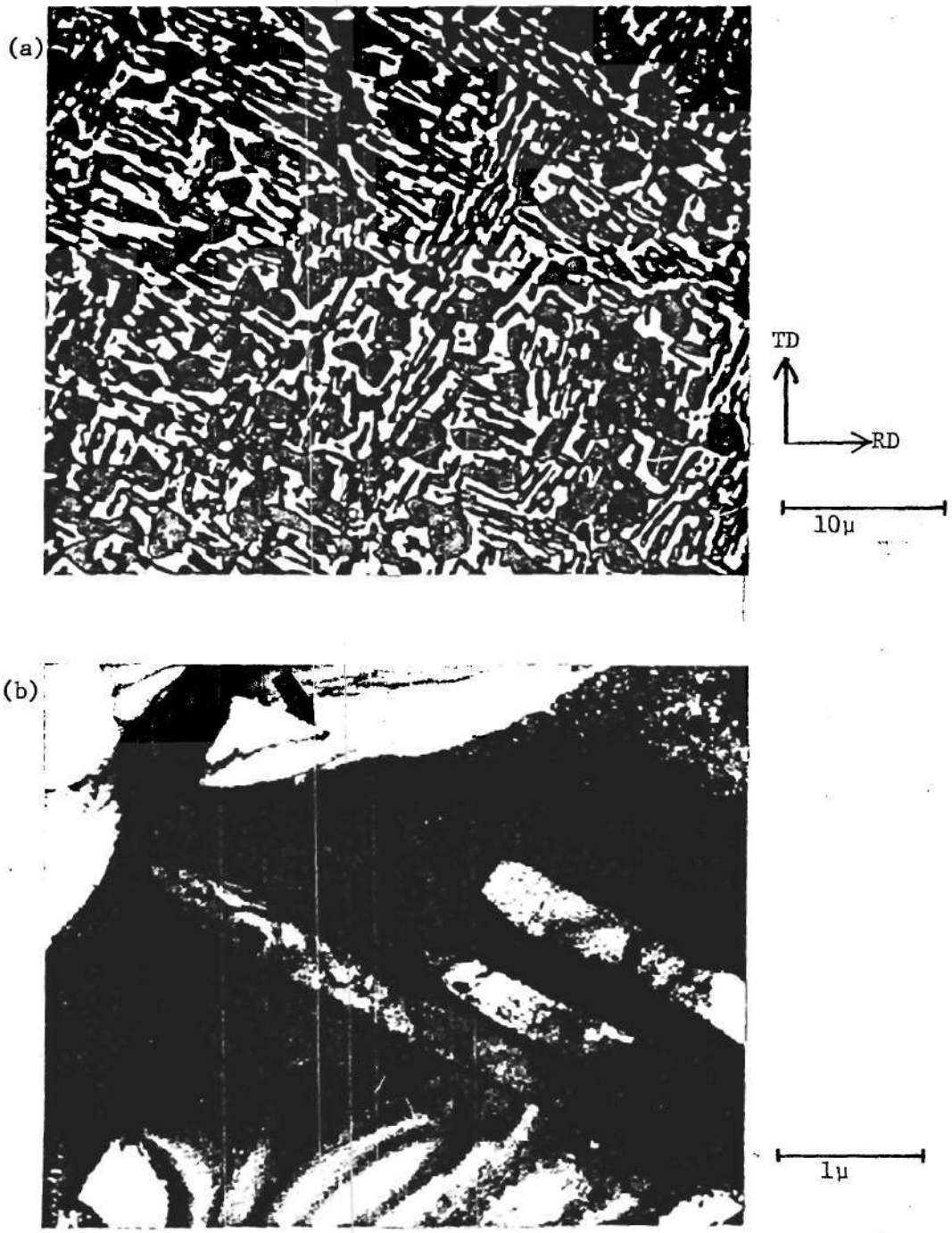

Figure 11. CX Alloy Water Quenched from 800°C, Aged 1 Hr. at 450°C: (a) optical, unpolarized, (b) TEM, typical area, possible precipitate (arrowed).

The plate thickness is approximately 1-3μ. Quantitative metallography shows the primary α phase volume fraction to be approximately 0.67. Figure 11b is a TEM of a typical area in the 800°C quenched and aged material. The plates can be seen to be featureless with some indication of homogeneous precipitation. The continuous network surrounding the α phase shows a tendency towards preferential etching which has been attributed to the presence of ω phase. Due to this preferential attack, these alloys did not thin uniformly and were not conducive to good transmission electron microscopy.

The results of x-ray diffraction studies on materials solutionized at 800°C are presented in Table 7 for both as-quenched and the quenched and aged conditions. These show the presence of hcp α phase and significant amounts of retained β or β + ω. The presence of ω in the as-quenched condition was indicated by a line at d=1.33 Å corresponding to the $(11\bar{2}2)$ ω line. After aging for 1 hour at 450°C, the d=1.33 Å line had increased in intensity slightly and a line corresponding to the ω $(11\bar{2}1)$ line at d=1.96 Å was noted (Table 7).

The results of x-ray quantitative analysis on a series of the CX alloy water quenched from temperatures ranging from 945°C to 800°C are listed in Table 8. The amount of retained β or β + ω increases with decreasing quenching temperature. At quenching temperatures less than 910°C significant amounts of β or β + ω are present while at higher temperatures only small amounts were detected. The presence of ω is supported by the d=1.33 Å, d=1.96 Å, diffraction lines and by the fact that several β peaks were observed to have distorted shapes indicating the possibility of superimposed β and ω peaks.

Table 8. Volume Fraction of Retained Beta in CX and CY Alloys in Various Conditions Obtained from Quantitative X-ray Diffractometry

Alloy and Condition	Heat Treat Temperature	Volume Fraction Retained Beta (in percent)	Volume Fraction Alpha (in percent)	Volume Fraction Beta after Aging (in percent)
CX Alloy Water Quenched	945	1.0	99+	--
	910	1.0	99+	0
	875*	19.6	80.4	--
	850	32.3	67.7	--
	825	11.7	88.3	--
	800	9.5	90.5	18.0
CX Alloy Furnace Cooled	910	4.4	95.6	--
	800	4.1	95.9	--
CY Alloy Water Quenched	945	0.0	100.0	--
	910	0.0	100.0	0.0
	875	1.7	98.3	--
	850	2.1	97.9	--
	825*	20.3	79.7	--
	800	18.6	81.4	17.6
CY Alloy Furnace Cooled	910	2.3	97.7	--
	800	2.7	97.3	--

*At quenching temperatures lower than these, the volume fractions indicate a trend only due to β and ω peak interference.

The microstructure exhibited by the furnace cooled materials had large equiaxed primary grains surrounded by a smaller amount of secondary grain boundary phase or transformed β. Some evidence of the prior β grains existed and were similar to the water quenched materials in size and shape.

The CX alloy furnace cooled from 910°C consisted of approximately 0.78 volume fraction primary α grains surrounded by a grain boundary phase of transformed β (Table 6) (Figure 12a). The transformed β phase consisted of very narrow regions generally less than 1μ in width and were difficult to resolve optically. The primary α grain size is 4μ as shown in Table 6. The TEM of Figure 12b shows a typical area in the furnace cooled material and illustrates that both phases are featureless. However, selected area diffraction taken in the β regions showed pronounced reciprocal lattice streaking which was thought to be due to very fine precipitates (Figure 13). Evidence of both homogeneous and preferred precipitation at grain boundaries was noted in these materials. Figure 14a shows a typical area in the primary α phase in which large homogeneous precipitates can be seen. Apparent preferred precipitation at the primary α and transformed β interface is also evident in Figure 14b.

The structure of the CX alloy furnace cooled from 800°C was similar to the 910°C furnace cooled material (Figure 15). However, the 10μ grain size was significantly larger than the 910°C furnace cooled sample and contained 0.80 volume fraction primary α phase. The observed d-spacing for CX alloy furnace cooled from 910°C and 800°C are listed in Table 9, along with calculated d-spacing for α Zr,

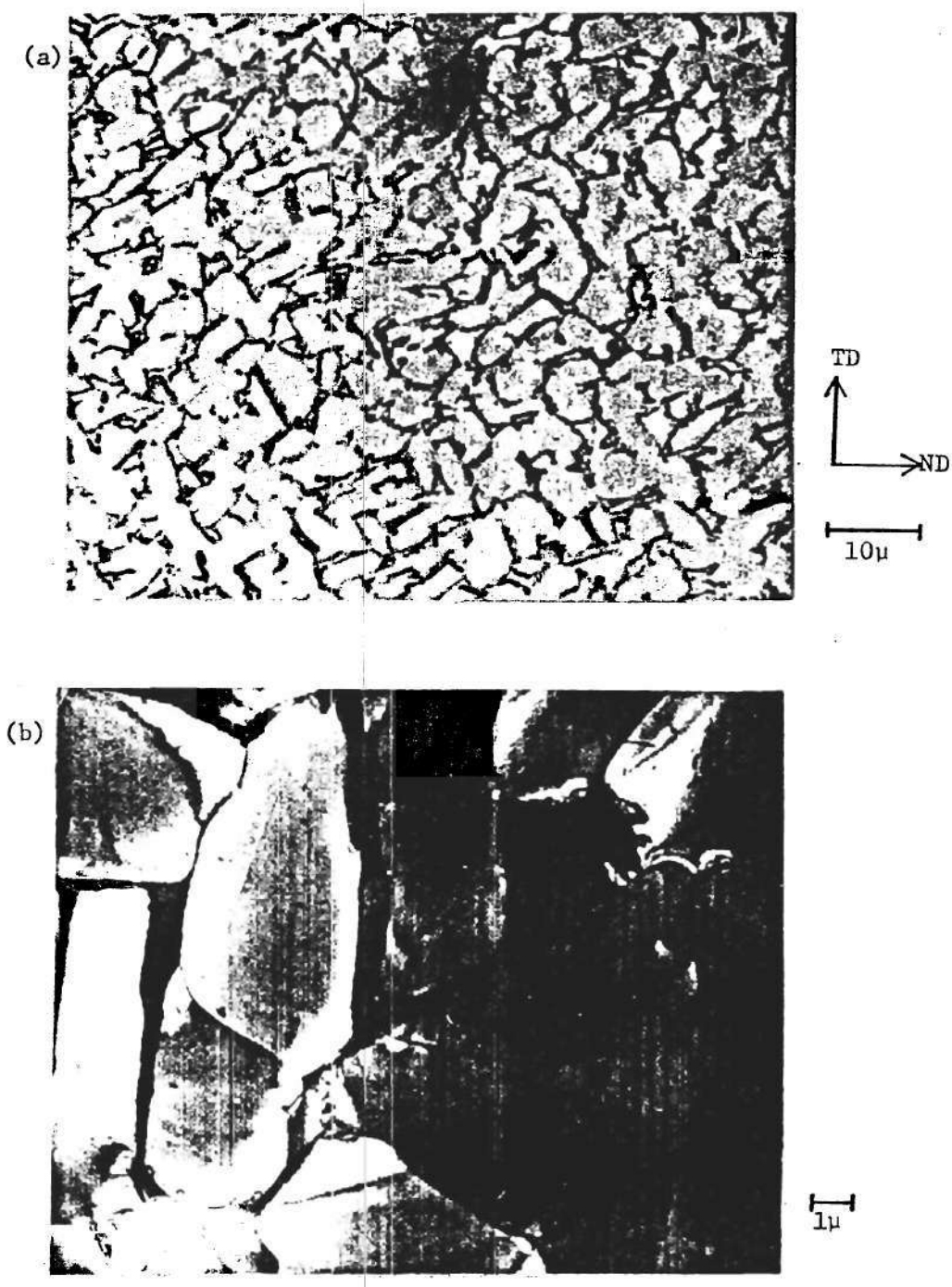

Figure 12. CX Alloy Furnace Cooled from 910°C: (a) optical micrograph, unpolarized, (b) TEM, typical area.

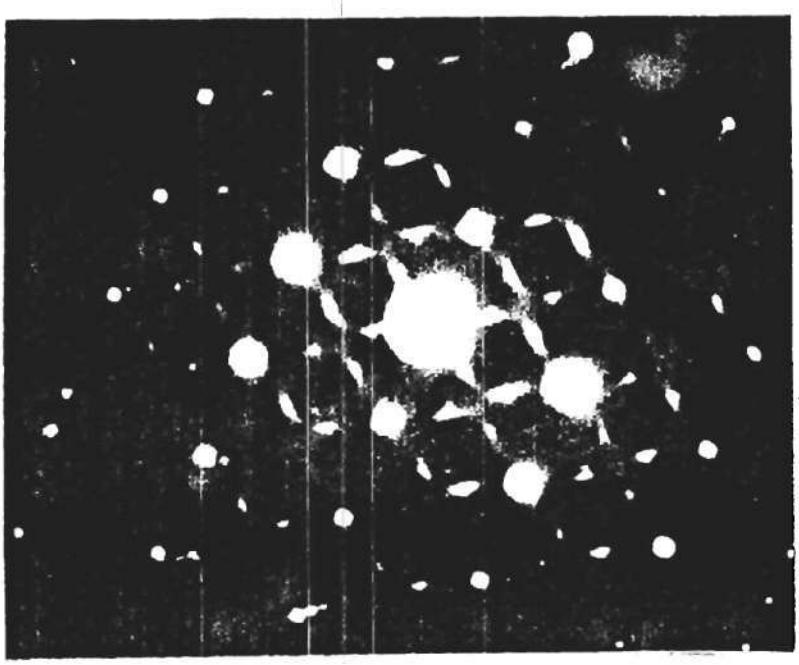

Figure 13. Selected Area Diffraction Pattern Taken in the Transformed β Region of the CX Alloy Furnace Cooled from 910°C. Shows Pronounced Reciprocal Lattice Streaking.

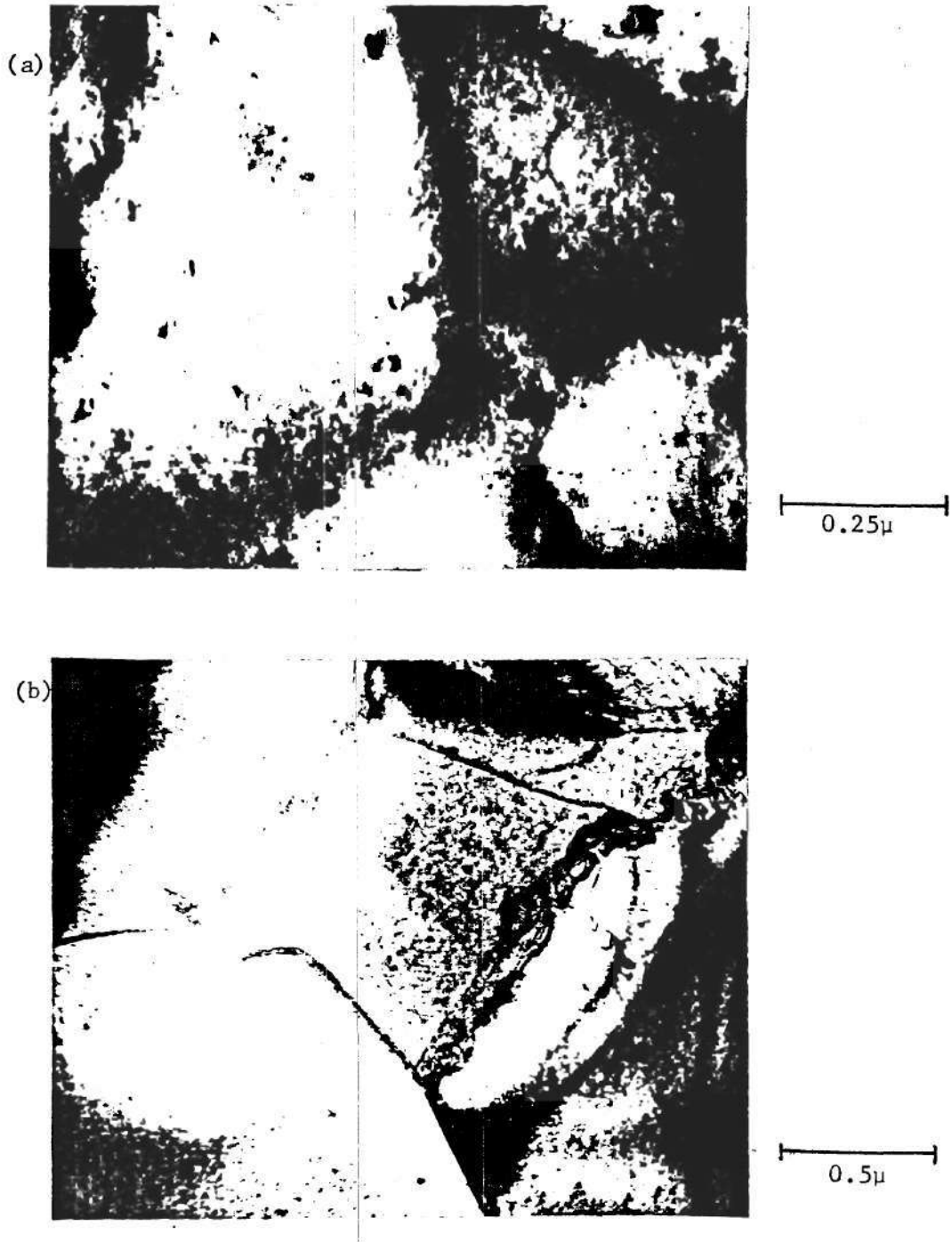

Figure 14. CX Alloy Furnace Cooled from 910°C: (a) homogeneous precipitates in primary α grain, (b) apparent preferred precipitation at primary α grain boundary.

Figure 15. CX Alloy Furnace Cooled from 800°C, Optical Micrograph Unpolarized.

Table 9. X-ray Data for CX and CY Furnace Cooled Alloys.

CX Alloy furnace cooled from 910°C		CX Alloy furnace cooled from 800°C		CY Alloy furnace cooled from 910°C		CY Alloy furnace cooled from 800°C		α Zr		β Zr		ω	
d,Å	I,cps	d,Å	I,cps	d,Å	I,cps	d,Å	I,cps	d,Å	hkil	d,Å	hkl	d,Å	hkil
2.80	550	2.80	300	2.80	900	2.80	550	2.798	$10\bar{1}0$				
2.59	6750	2.58	1950	2.58	3500	2.58	520	2.573	0002				
2.51	1800	2.51	400	2.50	600	2.51	210			2.51	110	2.51	$10\bar{1}1$, $11\bar{2}0$
2.47	5900	2.47	4700	2.46	2400	2.45	1825	2.459	$10\bar{1}1$				
1.90	170	1.90	320	1.89	300	1.89	90	1.894	$10\bar{1}2$			1.95	$11\bar{2}1$
1.79	25	1.78	25	1.77	25					1.78	200	1.78	$20\bar{2}1$
1.59	25	1.62	60	1.62	48	1.61	25	1.616	$11\bar{2}0$			1.68	$30\bar{3}0$
												1.54	0002
1.47	115	1.49	365	1.46	270	1.46	50	1.463	$10\bar{1}3$	1.45	211	1.45	$21\bar{3}1$
				1.45	35								
1.40	50	1.40	55	1.40	100	1.39	40	1.399	$20\bar{2}0$				
1.37	53	1.37	100	1.37	60	1.37	30	1.368	$11\bar{2}2$				
1.35	470	1.35	580	1.35	400	1.35	52	1.350	$20\bar{2}1$			1.31	$11\bar{2}2$, $30\bar{3}1$
1.29	50	1.29	135			1.28	25	1.287	0004				
1.25	68	1.25	25	1.25	400	1.25	220			1.26	220	1.26	$22\bar{4}0$
1.23	110	1.23	95	1.23	80			1.229	$20\bar{2}2$				
1.18	50	1.17	80	1.17	65			1.168	$10\bar{1}4$			1.16	$22\bar{4}1$

β Zr and ω. This shows β Zr to be present in both heat treatments; however, no indication of ω was found. Approximately 0.04 volume fraction retained β was indicated by quantitative x-ray analysis for both 910°C and 800°C solutionizing temperatures.

Figures 16 through 20 show the (0002) pole figures for the CX alloy in both water quenched and furnace cooled condition. The textures of 800°C quenched and aged and 800°C furnace cooled materials appear to be somewhat random. The 1000°C water quenched alloy shows a texture which is not similar to the expected rolled zirconium plate texture where (0002) poles are approximately 35° away from the normal direction toward the transverse direction.

The CY alloy water quenched from 1000°C and aged 1 hour at 450°C was very similar to the CX alloy in the same condition (Figures 21a and 21b). Its structure consisted of coarse martensite plates surrounded by much finer plates. The CY alloy did not differ noticeably from CX in platelet size or distribution (Table 10). The prior β grain size was evident in that the α' martensite plates consisted of colonies limited to one prior β grain. Figure 22 shows evidence of the homogeneous precipitation prevalent in the large α' martensite plates. These precipitates are assumed to be the same ones present in the CX alloy with the possibiliby of a Zr-Al phase existing. The presence of a large number of apparent stacking faults was noted in the CY alloy (Figure 23). None were noted in the CX alloy treated similarly. The only phase detected by x-ray diffraction was the hcp α phase.

The microstructure of the CY alloy water quenched from 910°C

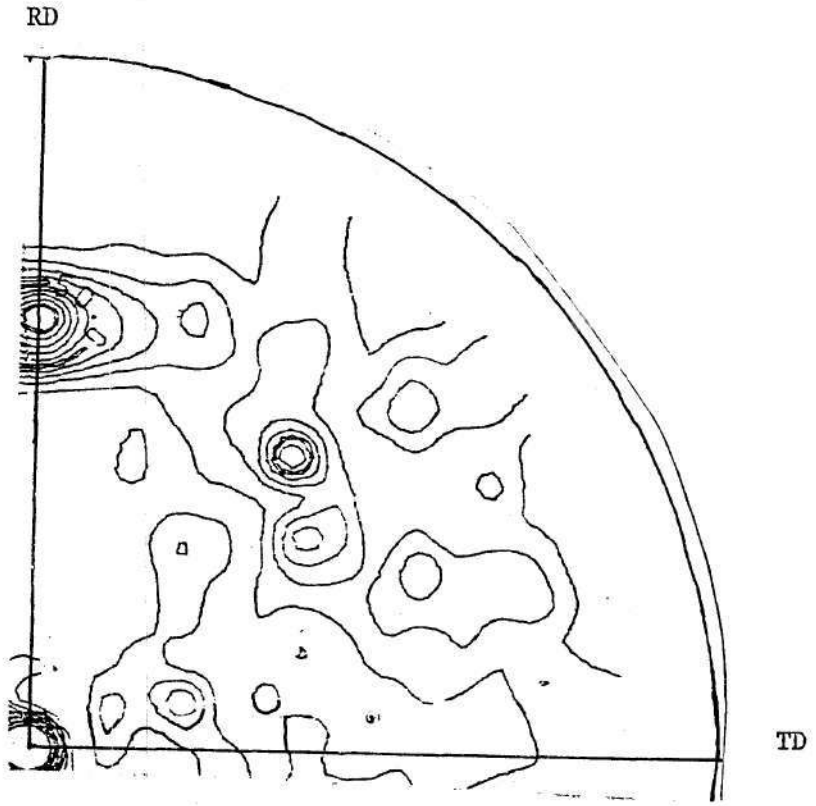

Figure 16. CX Alloy Water Quenched from 1000°C, Aged 1 Hr. at 450°C, (0002) Pole Figure.

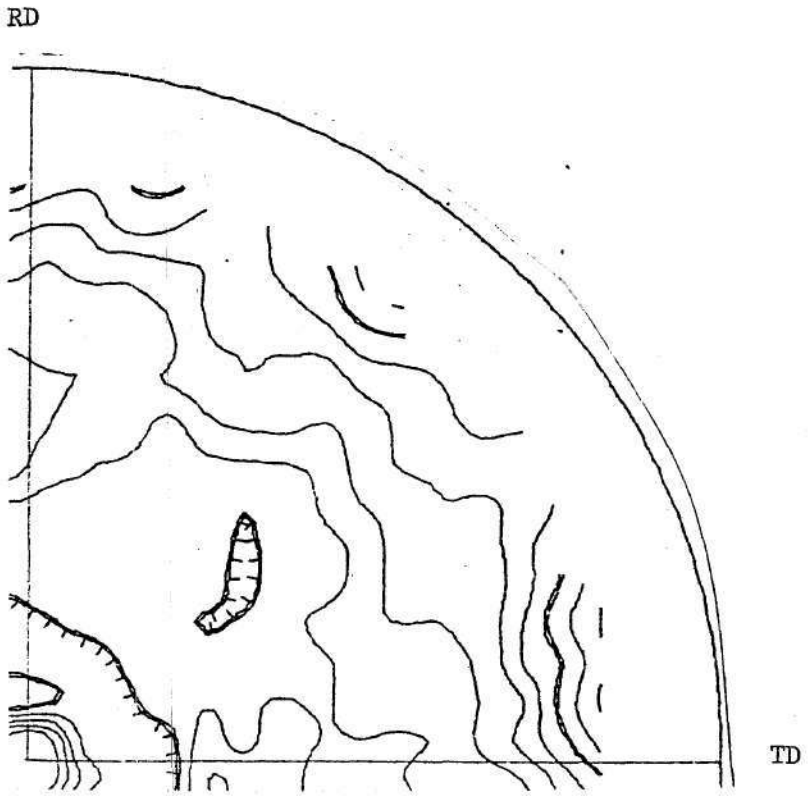

Figure 17. CX Alloy Water Quenched from 910°C, Aged 1 Hr. at 450°C, (0002) Pole Figure.

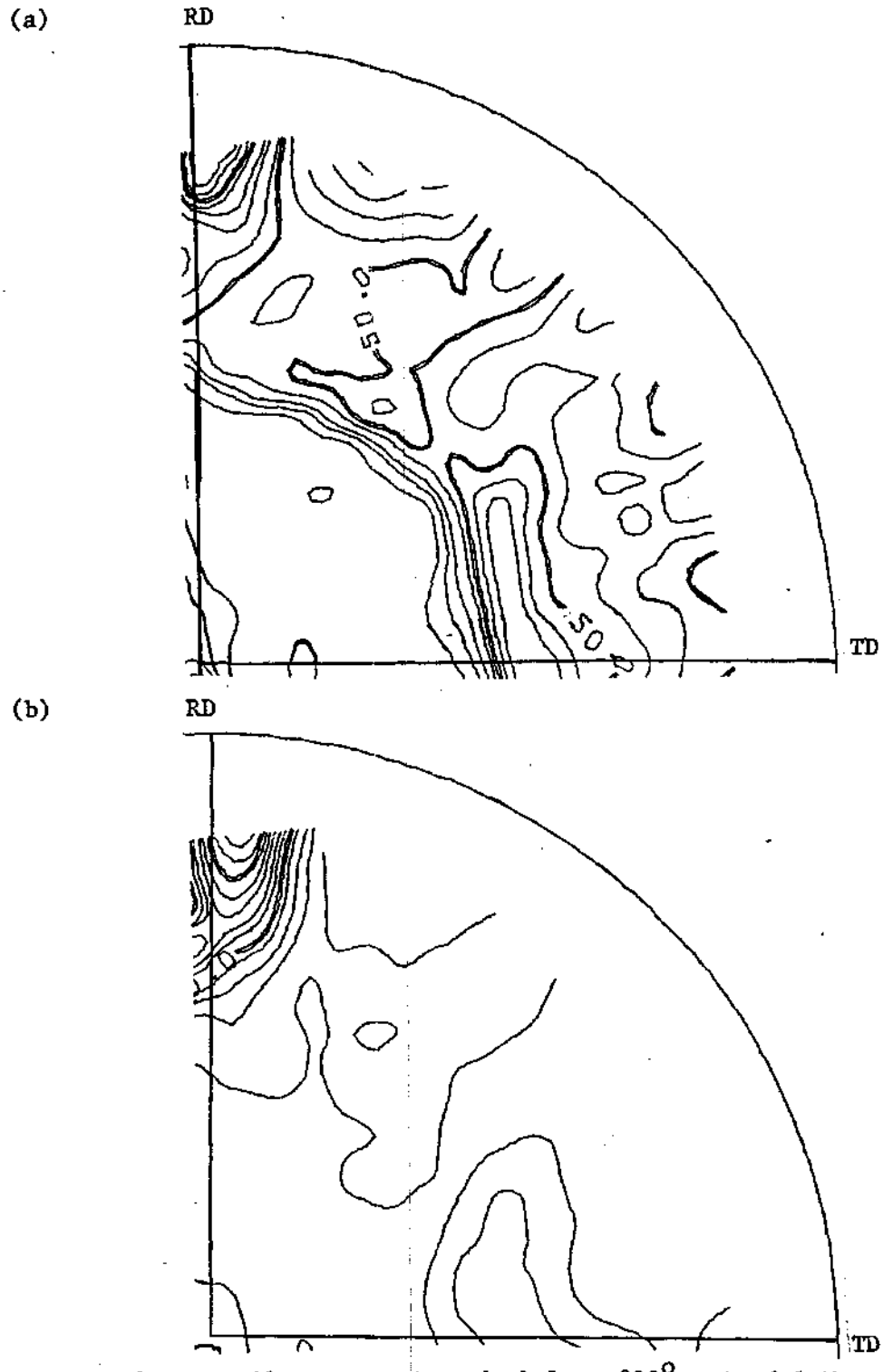

Figure 18. CX Alloy Water Quenched from 800°C, Aged 1 Hr. at 450°C: (a) (0002) pole figure, and (b) (110) pole figure.

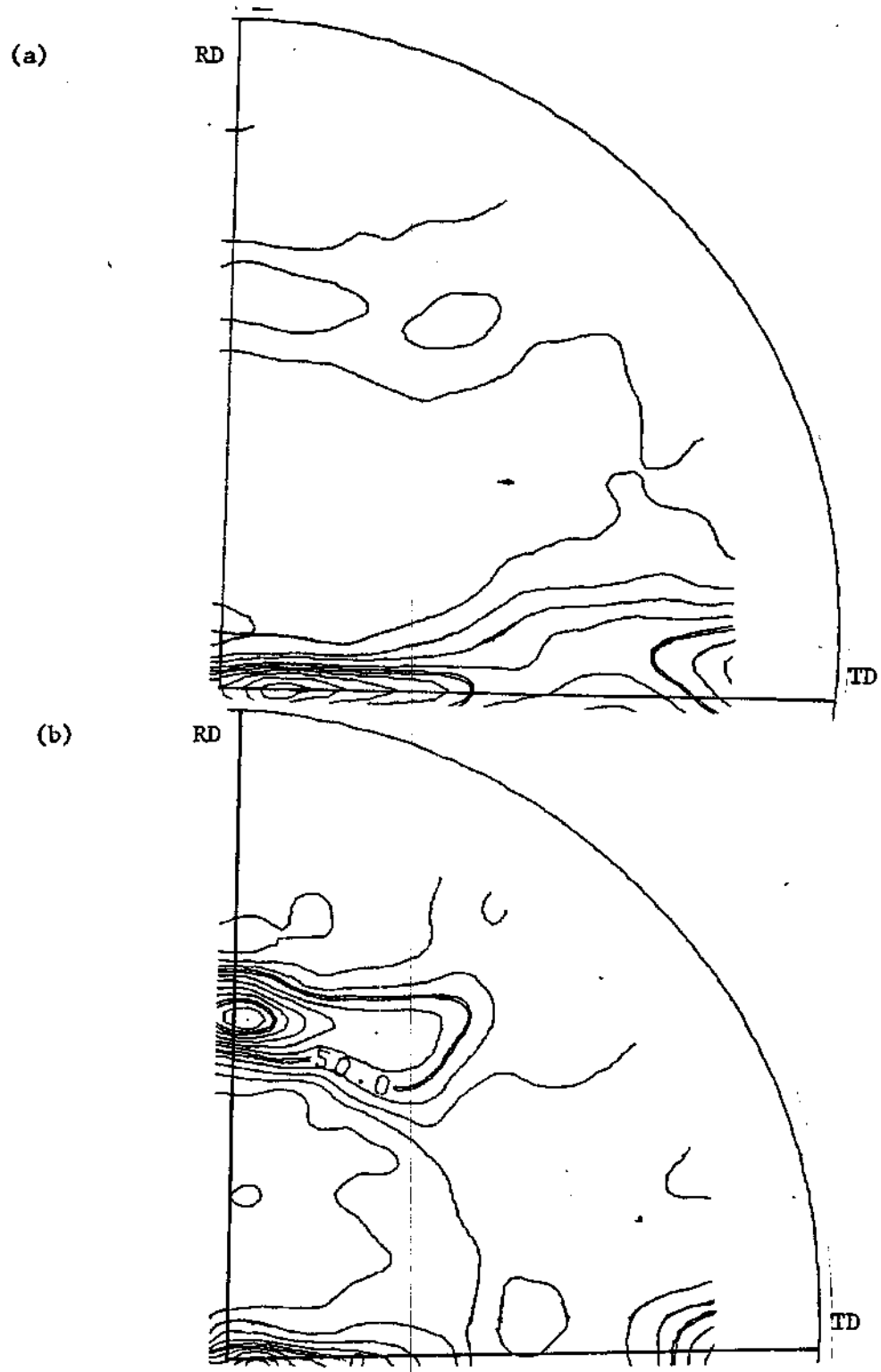

Figure 19. CX Alloy Furnace Cooled from 910°C: (a) (0002) pole figure, and (b) (110) pole figure.

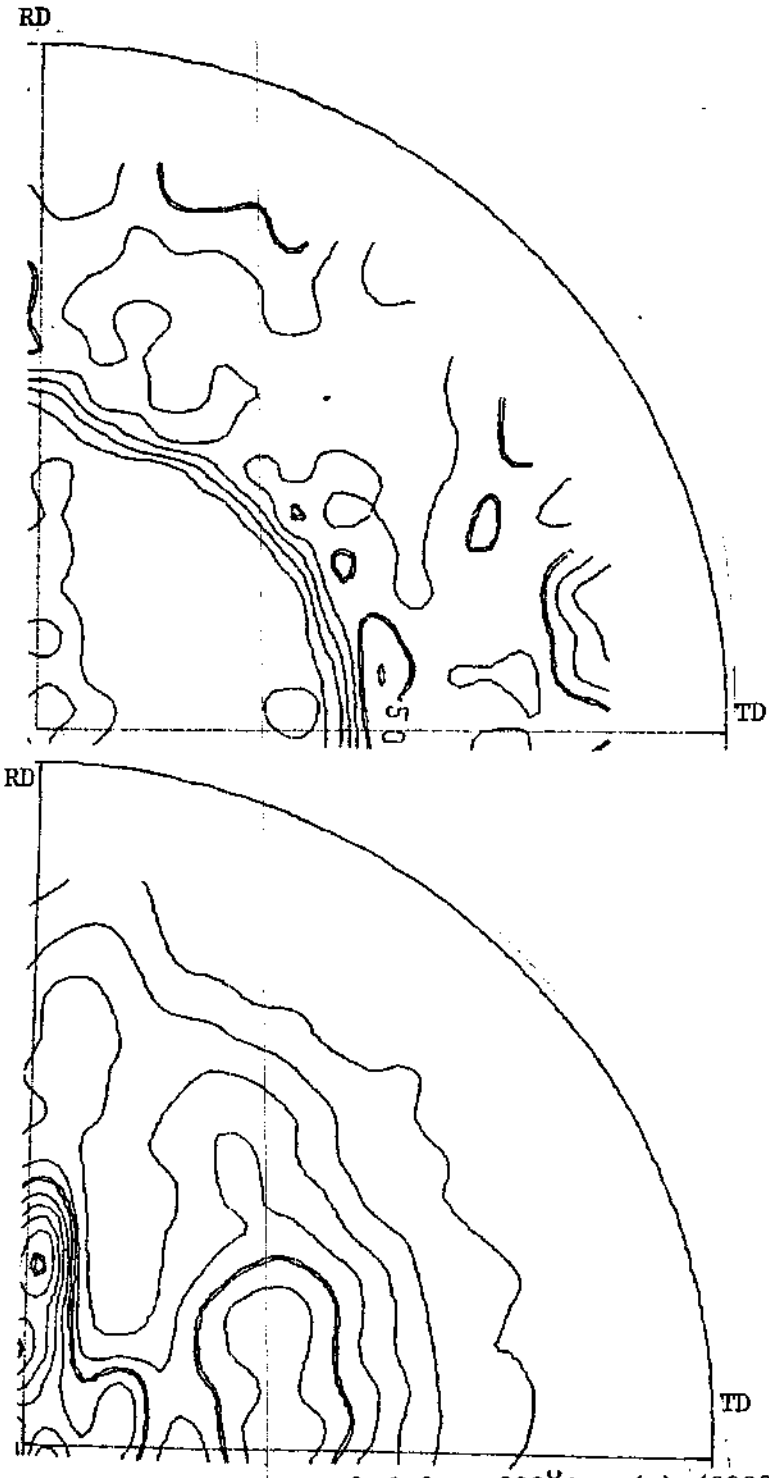

Figure 20. CX Alloy Furnace Cooled from 800°C: (a) (0002) alpha pole figure, and (b) (110) beta pole figure.

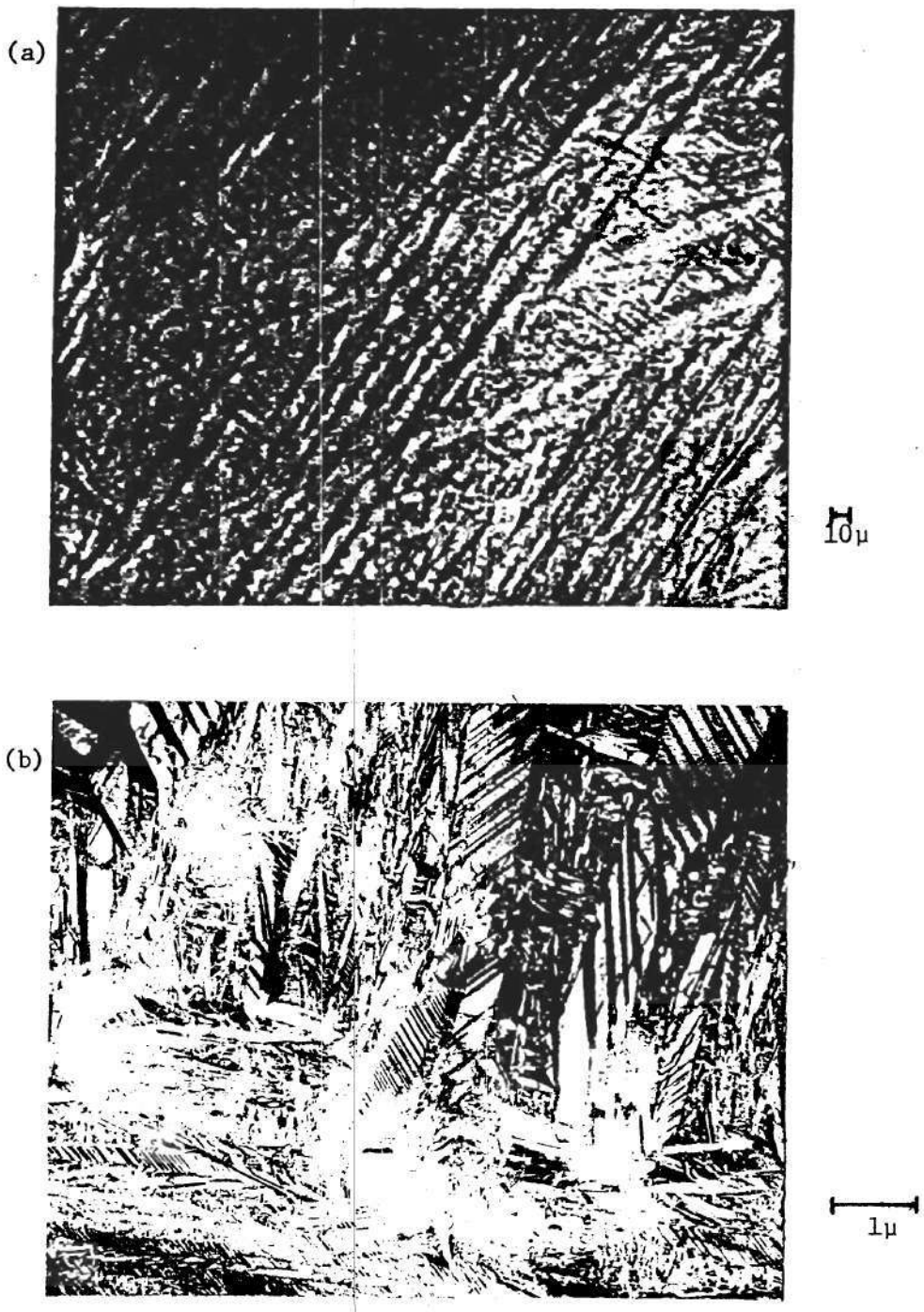

Figure 21. CY Alloy Water Quenched from 1000°C, Aged 1 Hr. at 450°C: (a) optical micrograph, unpolarized 170X, and (b) TEM, typical area.

Table 10. CY Alloy Quantitative Metallography

Alloy and Heat Treatment	Volume Percent Isothermal α	Volume Percent Athermal α'	Isothermal α Grain Size	Athermal α' Grain Size	Athermal α' Twin Size	Athermal α' Twin Spacing
CY water quenched from 1000°C aged 1h at 450°C	--	100	--	Coarse-2.0mm length x 1-3 μ width. Fine-5-10μ length x 0.5μ to 1000Å width.	Coarse-1000-5000Å. Fine-1000-3000Å.	1000-3000Å
CY water quenched from 910°C aged 1h at 450°C	22	78	7.0μ	Coarse-5-20μ length, 1μ width. Fine-1μ length, 1000Å width.	500-2000Å	500-3000Å
CY water quenched from 800°C aged 1h at 450°C	51	49	4.3μ	--	--	--
CY furnace cooled from 910°C	21	79	2.8μ	--	--	--
CY furnace cooled from 800°C	25	75	6μ	--	--	--

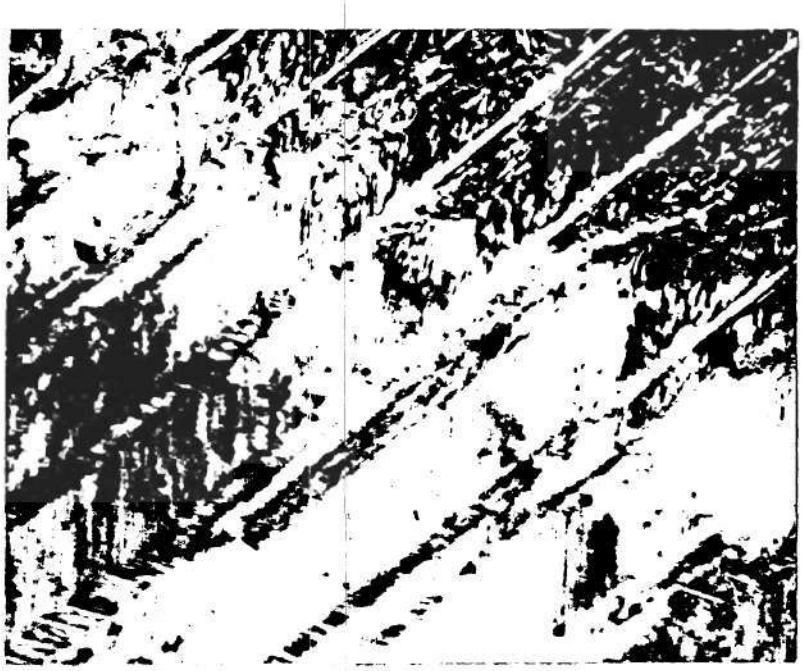

Figure 22. CY Alloy Water Quenched From 1000°C, Aged 1 Hr. at 450°C. Homogeneous Precipitation in Large Martensite Plates.

Figure 23. Stacking Faults in the CY Alloy Quenched from 1000°C.

and aged 1 hour at 450°C is similar to that of the similarly treated CX alloy (Figures 24a and 24b) and consists of equiaxed primary α grains in a matrix of α' martensite plates. The platelet size and size distribution were approximately the same as the CX alloy. Table 10 shows the volume fraction of primary α to be slightly greater than in the CX alloy. Also the primary α grain size of 10μ was significantly larger. The homogeneous precipitation noted in all other heat treatments was also found in the 910°C quenched and aged materials (Figure 25). X-ray diffraction showed only hcp α phase present in the CY alloy as-quenched from 910°C (Table 11). After aging for one hour at 450°C a weak line appeared at d=1.34 Å, corresponding to the ω $(11\bar{2}2)/(211)$ β Nb line. This behavior is similar to the CX alloy except for the trace amounts of retained β or β+ω noted in the as-quenched CX alloy.

The structure of the CY alloy water quenched from 800°C and aged 1 hour at 450°C was distinctly different from any of the other heat treatments. Optical microscopy showed the structure to consist of approximately 0.50 volume equiaxed light and dark phases (Figure 26a) (Table 10). The dark phase is assumed to be primary α based on its chemical etching characteristics. TEM shows the lighter phase to consist of discreet equiaxed grains approximately 4μ size (Figure 26b). The lighter phase is assumed to be primary α based on its electropolishing characteristics as compared with previous work. The second phase in this heat treatment was similar in character to the continuous network surrounding the primary α plates of the CX alloy in the same condition; however, this phase was not continuous. The apparent

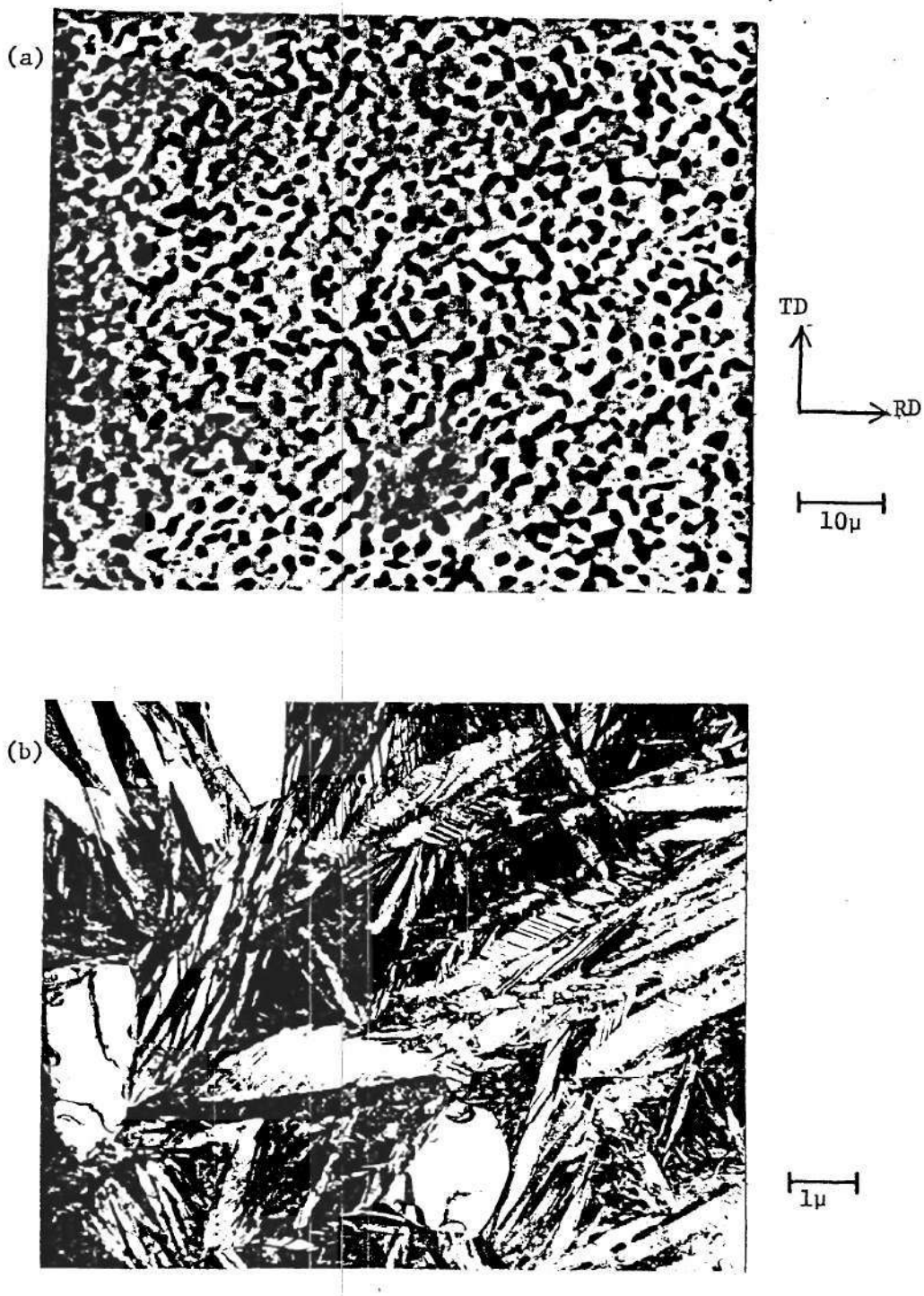

Figure 24. CY Alloy Water Quenched from 910°C, Aged 1 Hr. at 450°C: (a) optical micrograph, unpolarized, and (b) TEM.

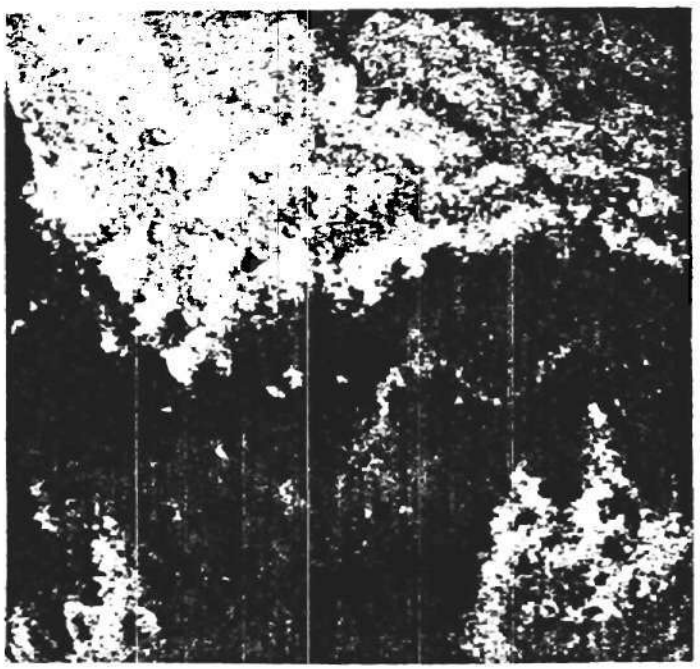

0.25μ

Figure 25. Homogeneous Precipitation in the CY Alloy Water Quenched from 910°C and Aged 1 Hr. at 450°C.

Table 11. Observed d-spacing for the CY Alloy in the Water Quenched Condition

910°C water quench		800°C water quench		910°C quenched/aged		800°C quenched/aged		α Zr			β Zr		ω	
d,Å	I,cps	d,Å	I,cps	d,Å	I,cps	d,Å	I,cps	d,Å	hkil		d,Å	hkl	d,Å	hkil
2.80	425	2.79	470	2.80	320	2.80	1200	2.798	$10\bar{1}0$					
2.78	250			2.77	100									
2.58	1275	2.57	675	2.58	500	2.58	300	2.573	0002					
		2.51	1357			2.52	2300				2.51	110	2.51	$10\bar{1}1,11\bar{2}0$
2.47	2000	2.45	1750	2.45	2100	2.46	4700	2.459	$10\bar{1}1$					
				1.89	180	1.96	30						1.95	$11\bar{2}1$
1.89	100	1.89	145			1.89	420	1.894	$10\bar{1}2$					
		1.78	75			1.79	110				1.78	200	1.78	$20\bar{2}1$
						1.76	30						1.68	$30\bar{3}0$
1.62	35	1.62	73	1.62	140			1.616	$11\bar{2}0$				1.54	0002
1.46	175	1.46	228	1.46	250	1.46	500	1.463	$10\bar{1}3$		1.45	211	1.45	$21\bar{3}1$
		1.45	170	1.45	140									
1.40	50	1.39	45	1.39	50	1.39	140	1.399	$20\bar{2}0$					
1.36	150	1.36	370	1.36	200	1.37	30	1.368	$11\bar{2}2$					
1.35	225	1.35	290	1.35	260	1.35	370	1.35	$20\bar{2}1$					
		1.33	25	1.34	80								1.31	$11\bar{2}2,30\bar{3}1$
1.29	150	1.28	48	1.28	30	1.28	140	1.287	0004					
		1.26	80			1.26	210				1.26	220	1.26	$22\bar{4}0$
		1.23	45	1.23	40	1.23	80	1.239	$20\bar{2}2$					
		1.17	23	1.17	40	1.17	60	1.168	$10\bar{1}4$				1.16	$22\bar{4}1$

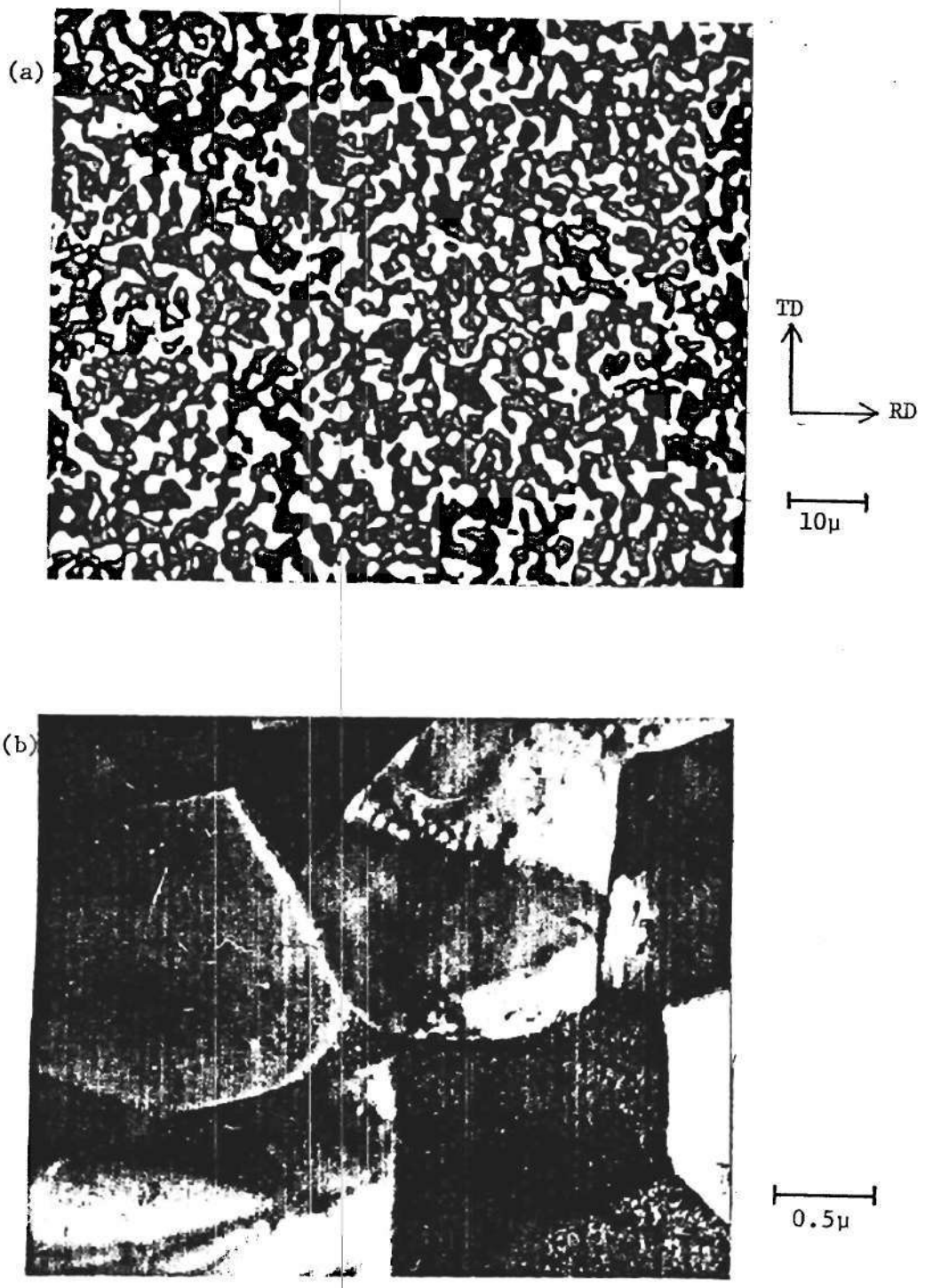

Figure 26. CY Alloy Water Quenched from 800°C, Aged 1 Hr. at 450°C: (a) optical micrograph, unpolarized, and (b) TEM, typical area.

preferential etching attributed to the presence of ω was also noted in this phase (Figure 26b).

The observed d-spacing for the CY alloy solutionized at 800°C both in the as-quenched and the quenched and aged conditions are presented in Table 11. Both hcp α and retained β or β + ω lines are present. The line at d=1.33 Å corresponds to the $\omega(11\bar{2}2)$ line. After aging for 1 hour at 450°C an additional line was observed at d=1.96 Å corresponding to the ω(1121) line. During this aging process the d=1.33 Å line disappeared.

Table 8 shows the results of x-ray quantitative analysis of the CY alloy quenched from temperatures ranging from 943°C to 800°C. For quenching temperatures greater than 875°C no retained β was found. However, as in the CX alloy at lower quenching temperatures, increasing amounts of retained β or β + ω were noted. The temperature at which β is first retained is somewhat lower in the CY alloy than in the CX.

Figures 27a and 27b are typical areas in the CY alloy furnace cooled from 910°C. This shows a structure consisting of large equiaxed primary α grains surrounded by a grain boundary phase of transformed β. The primary α consisted of approximately 0.80 volume fraction of the total structure (Table 10). The grain size in the 800°C furnace cooled materials was 2.8μ (Table 10). This is smaller than the CX alloy in the same condition. Figure 27b shows evidence of preferred precipitation at the primary α/transformed β interface. The CY alloy furnace cooled from 800°C was similar to the 910°C furnace cool and is shown in Figure 28. The amount of primary α is approximately the same as in the 910°C furnace cool (Table 10). The grain size in this

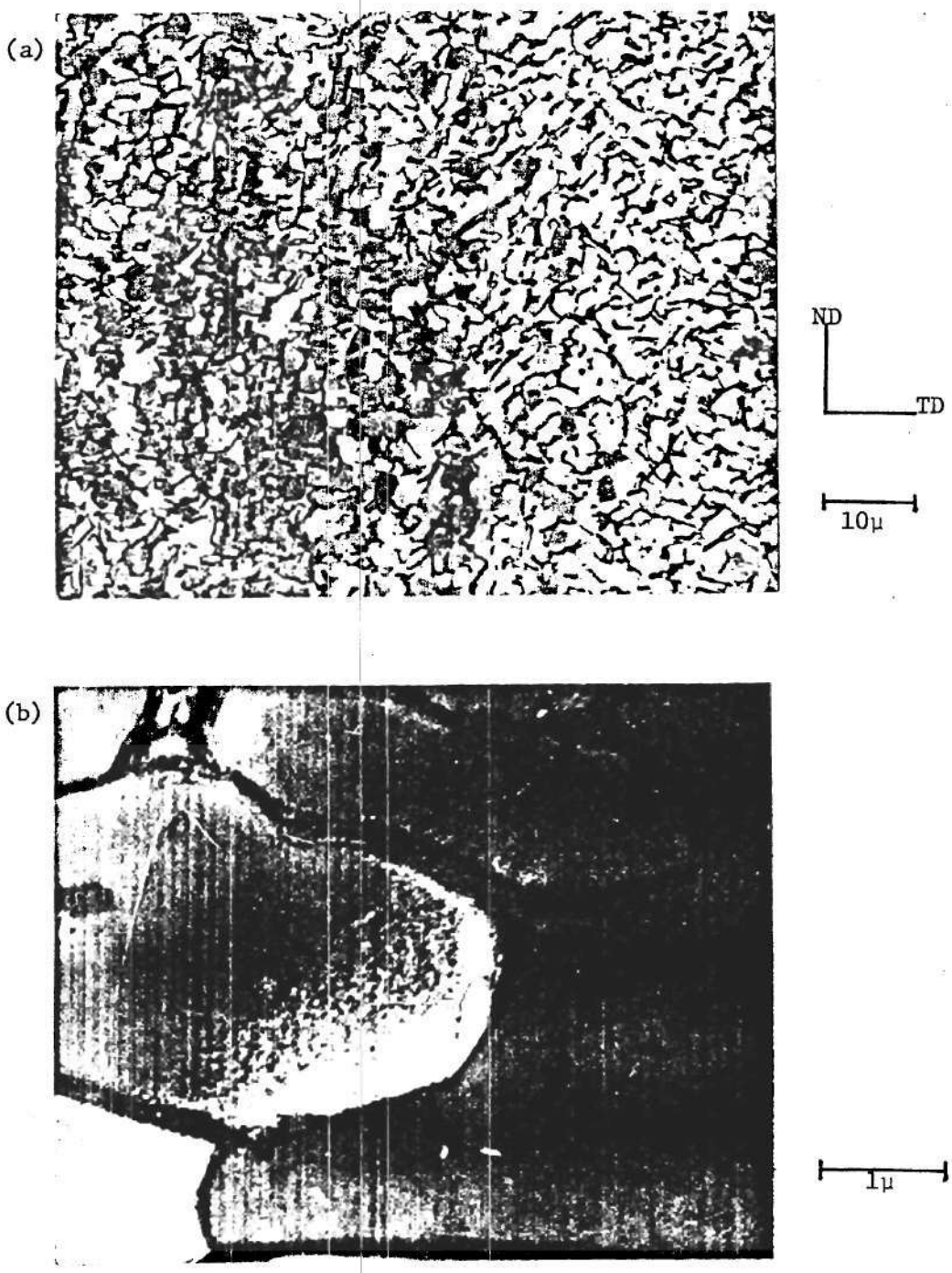

Figure 27. CY Alloy Furnace Cooled from 910°C: (a) optical micrograph, unpolarized, and (b) TEM, typical area.

Figure 28. CY Alloy Furnace Cooled from 800°C, Optical Micrograph, Unpolarized.

heat treatment was the largest of all at 10μ. Table 11 lists the "d" spacings for the CY alloy furnace cooled from 910°C and 800°C. Both hcp α and retained β lines are present. Quantitative x-ray analysis shows the amount of retained β to be 2.5% volume which is approximately half of that noted in the CX alloy similarly treated. The texture exhibited by the water quenched CY alloys was similar to the CX alloys as shown by Figures 29-32. $(10\bar{1}1)$ pole figure of Figure 32 can be derived from (0002) pole figure of Figure 20.

Mechanical Properties

The results of aging kinetic studies for the 910°C and 800°C water quenched samples are presented in Figures 33 through 35 along with aging curves for 1000°C water quench of Williams, et al[4]. These curves show similar variation for the 910°C and 800°C with maximum hardness occurring at approximately 1 hour of aging. The as-quenched hardness is similar in the CX and CY alloys in both quenching temperatures (Table 12); however, the maximum hardness is significantly higher in the 910°C quenched material. The CX alloy quenched from 1000°C showed similar behavior to the CX and CY alloy water quenched from 910°C and 800°C with maximum hardness occurring during aging at 450°C after about 1 hour. The CY alloy quenched from 1000°C, however, showed a much slower aging behavior with maximum hardness occurring at about 10 hours. Table 12 shows that the 910°C and 1000°C water quenched maximum hardness is approximately the same for the CX alloy and for the CY quenched from 910°C. The CY alloy water quenched from 1000°C had a significantly higher maximum hardness. The 1000°C as-quenched hardness of the CX and CY alloys was the same but was significantly harder than for the lower temperature quench.

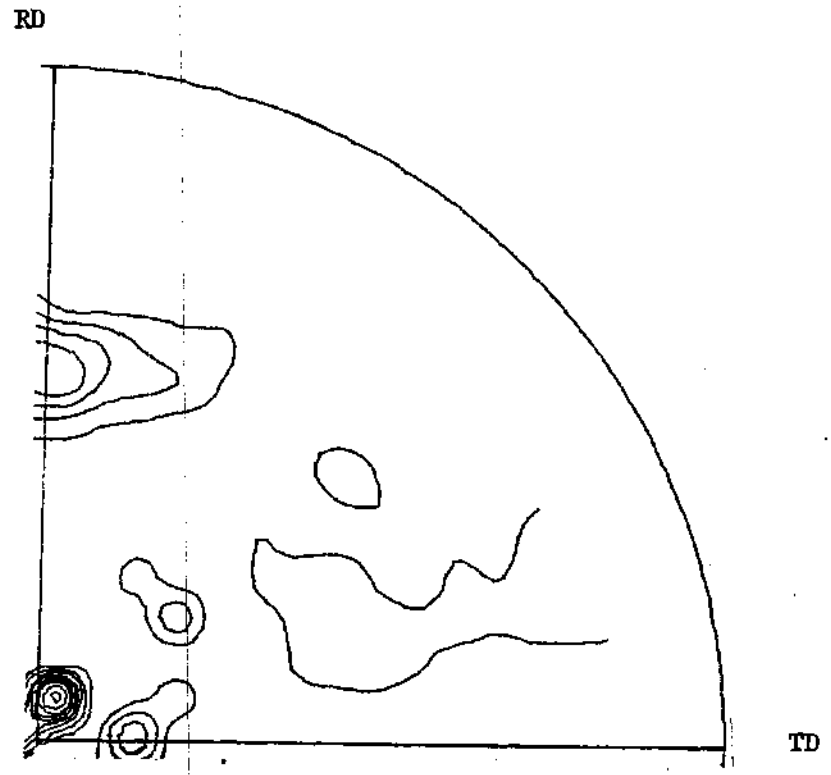

Figure 29. CY Alloy Water Quenched from 1000°C, Aged 1 Hr. at 450°C, (0002) Pole Figure.

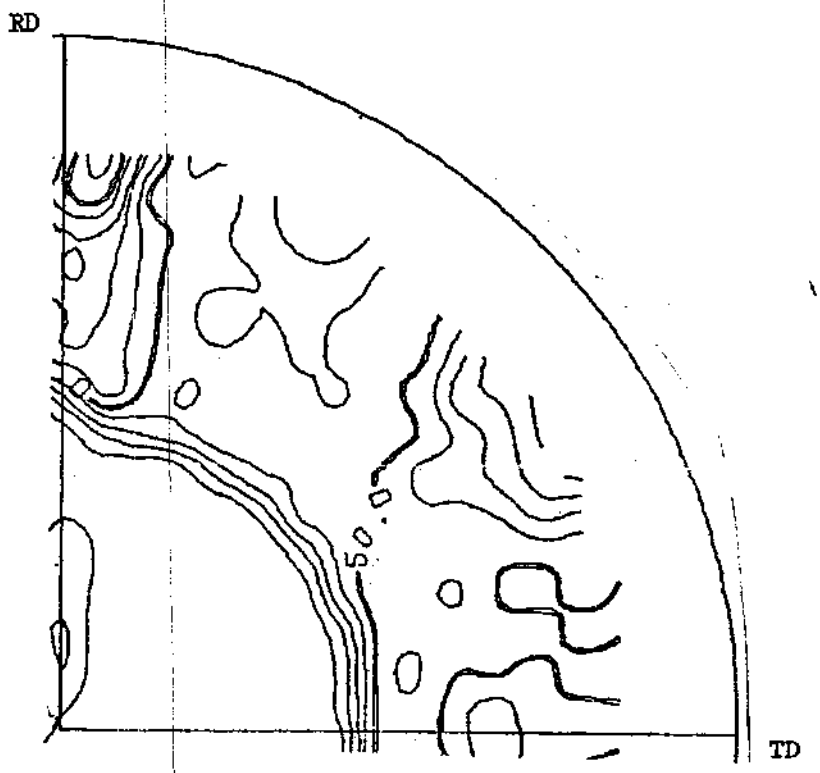

Figure 30. CY Alloy Water Quenched from 800°C, Aged 1 Hr. at 450°C, (0002) Pole Figure.

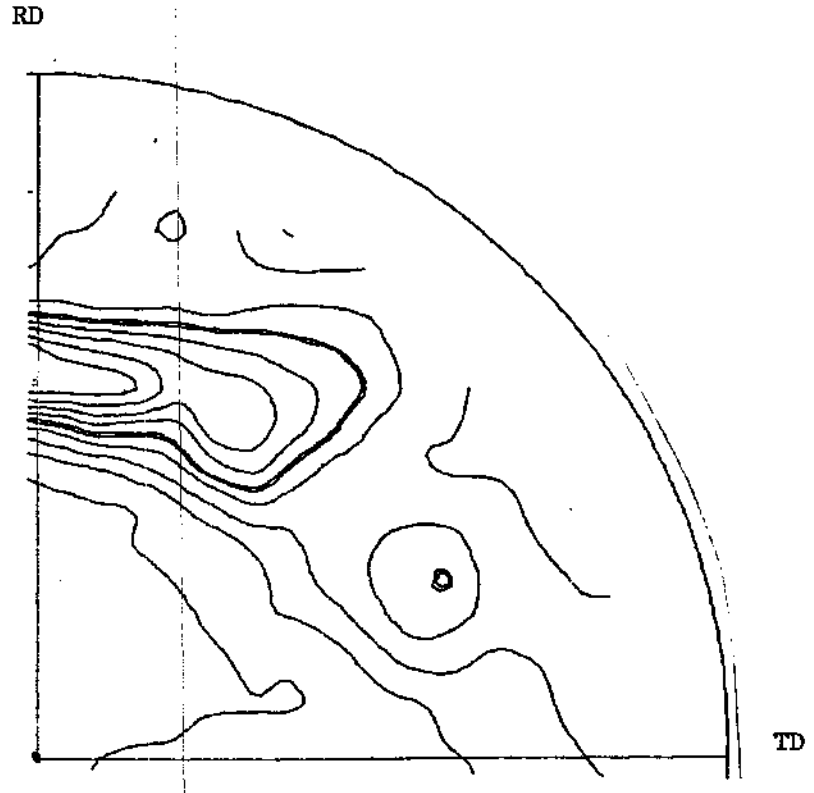

Figure 31. CY Alloy Furnace Cooled from 910°C, $(10\bar{1}1)$ Pole Figure.

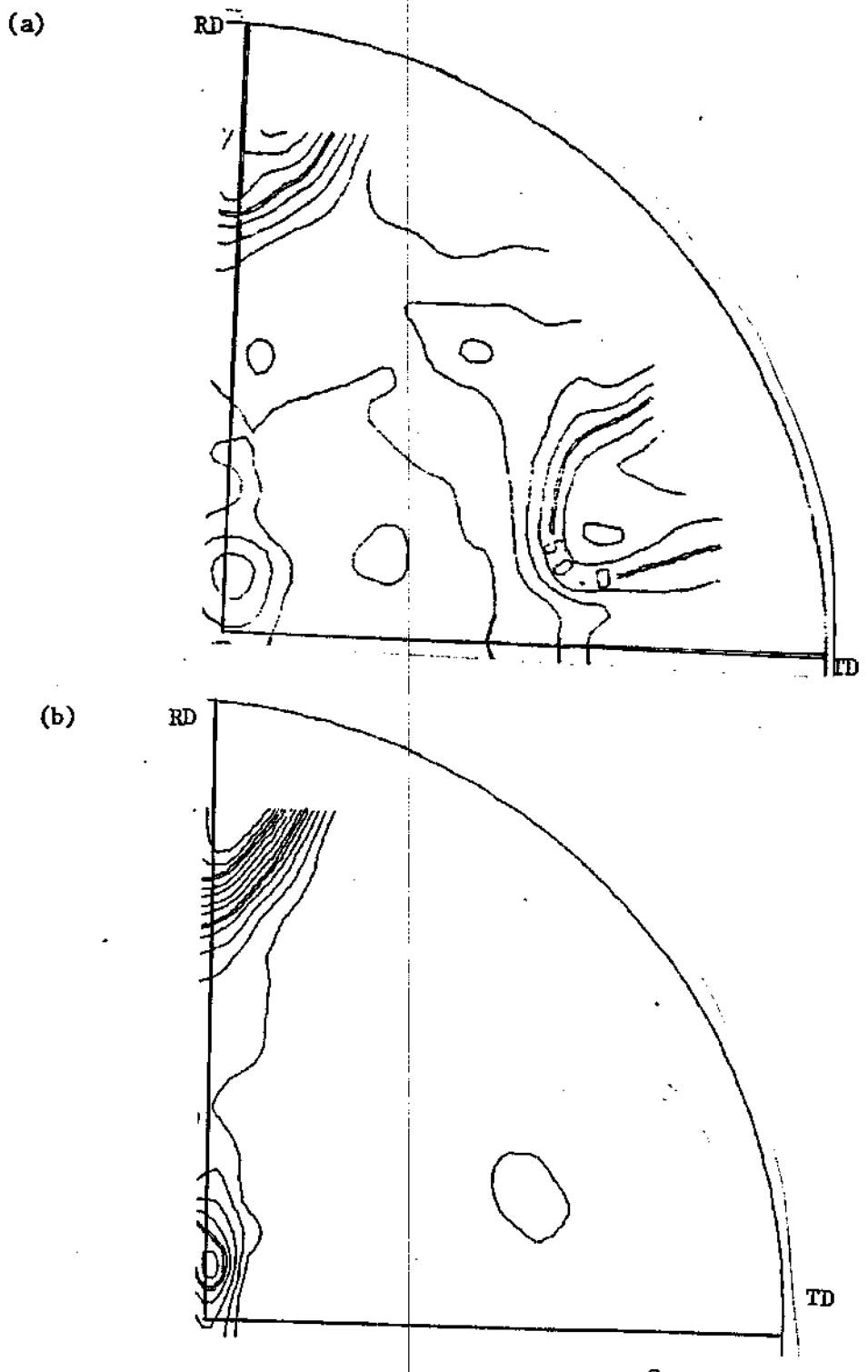

Figure 32. CY Alloy Furnace Cooled from 800°C: (a) (0002) pole figure, and (b) (110) pole figure.

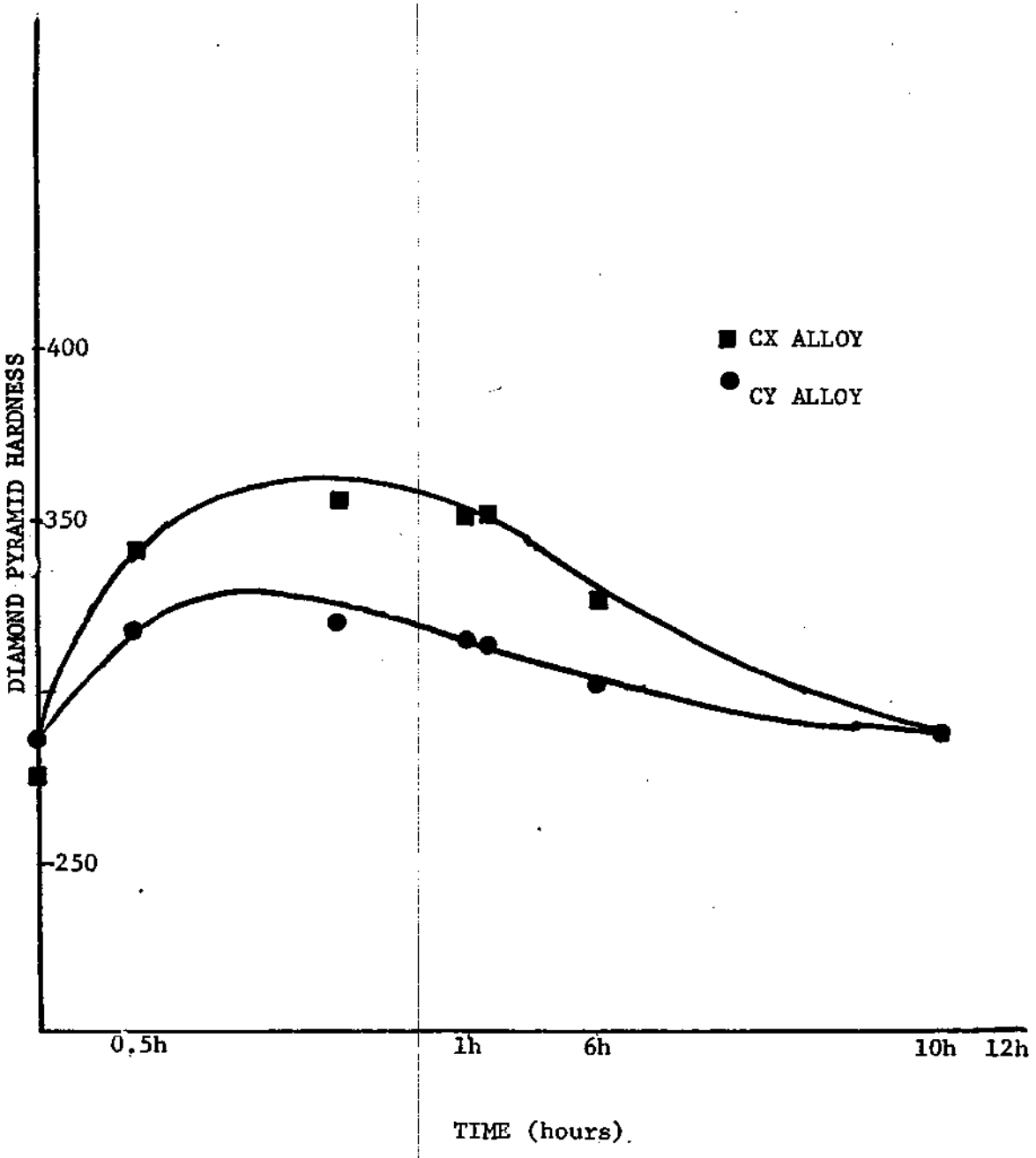

Figure 33. CX and CY Alloys, Water Quenched from 800°C, Aged at 450°C.

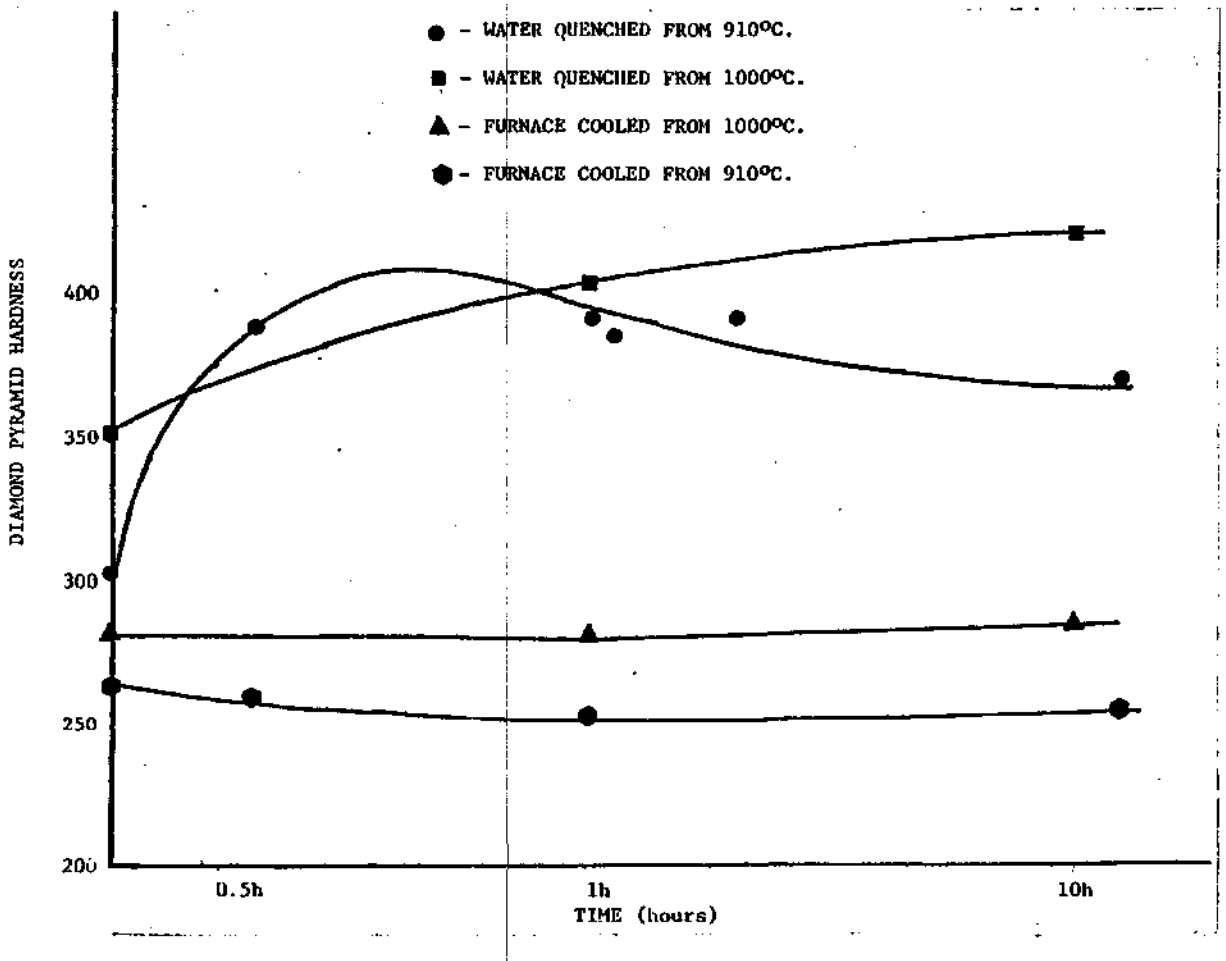

Figure 34. CY Alloy Aged at 450°C.

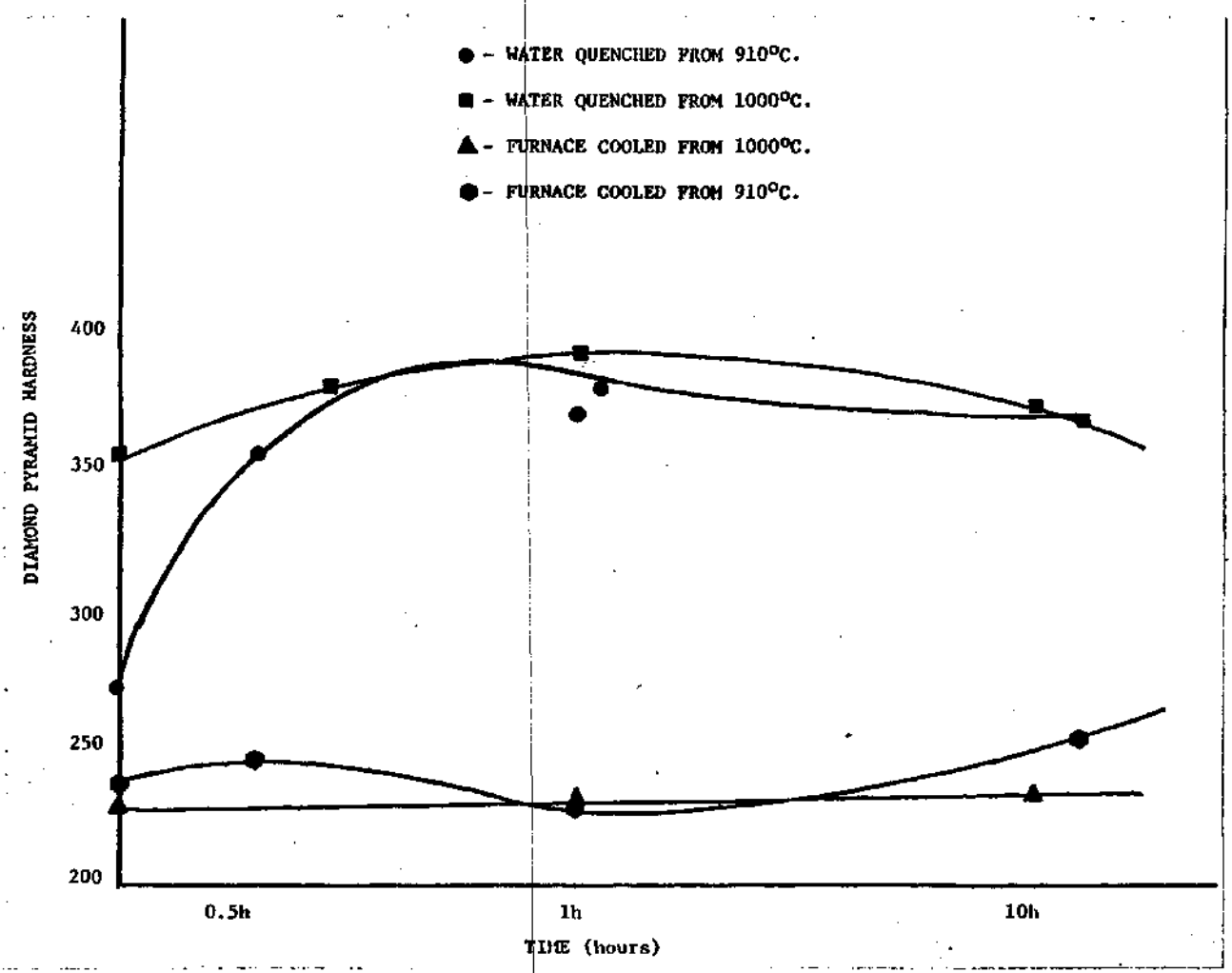

Figure 35. CX Alloy Aged at 450°C.

Table 12. DPH of CX and CY Alloys

Alloy	Water quenched from 1000°C		Water quenched from 910°C		Water quenched from 800°C		Furnace cooled from 1000°C(8)	Furnace cooled from 910°C	Furnace cooled from 800°C
	as quenched	aged 1h at 450°C	as quenched	aged 1h at 450°C	as quenched	aged 1h at 450°C			
CX	314	390	273	385	271	330	247	237	227
CY	314	387	296	390	276	352	280	264	262

The materials furnace cooled from 910°C and 800°C showed a lower hardness than the water quenched and aged materials and had little or no aging response (Figures 34 and 35, Table 12). The CY alloy exhibited higher hardness in all furnace cooled conditions than the CX alloy in similar conditions. Table 13 lists the results of hardness versus quenching temperature studies. These show only slight variation in hardness with changes in quenching temperature. Considering the error involved in the measurements the DPH hardness is approximately constant with quenching temperature.

The results of tensile tests performed in argon at 350°C are presented in Table 14. There were significant differences in the strength for the two alloys and heat treatments. The furnace cooled materials exhibited much lower strengths and higher ductility than the water quenched materials. The CY alloy showed higher strengths in the furnace cooled condition than did the CX alloy. The strength and ductility of the furnace cooled materials did not change significantly with solutionizing temperature. The water quenched alloy showed excellent strengths but very low ductility, generally less than 5% elongation at fracture (Table 14). The 910°C water quenched material exhibited a higher strength than both the 1000°C and the 800°C quenched material. The alloy quenched/aged from 800°C exhibited the lowest strengths of the quenched/aged materials. Even so, these were significantly higher than the furnace cooled strengths.

Deformation

Figures 36a and 36b are macrographs of tensile samples

Table 13. DPH of CX and CY Alloys in the Water Quenched Condition

	Quenching Temperature					
Alloy	945°C	910°C	875°C	850°C	825°C	800°C
CX	303	273	316	282	308	271
CY	322	296	309	322	308	276

Table 14. Results of Tensile Tests Conducted at 350°C in Argon for CX and CY Alloys

Alloy/Heat Treatment	UTS@350°C lb/in^2	0.2%@350°C lb/in^2	Elongation at Fracture %
Water quenched from 1000°C aged 1 hour at 450°C			
CX	141,769	134,223	4
CY	152,300	143,443	2
Water quenched from 910°C aged 1 hour at 450°C			
CX	152,364	139,358	2.2
CY	171,111	154,575	2.9
Water quenched from 800°C aged 1 hour at 450°C			
CX	81,300	36,471	<10
CY	114,800	64,800	<10
Furnace cooled from 910°C			
CX	57,674	43,924	19
CY	71,410	55,180	18
Furnace cooled from 800°C			
CX	51,500	43,000	18
CY	74,600	68,000	16

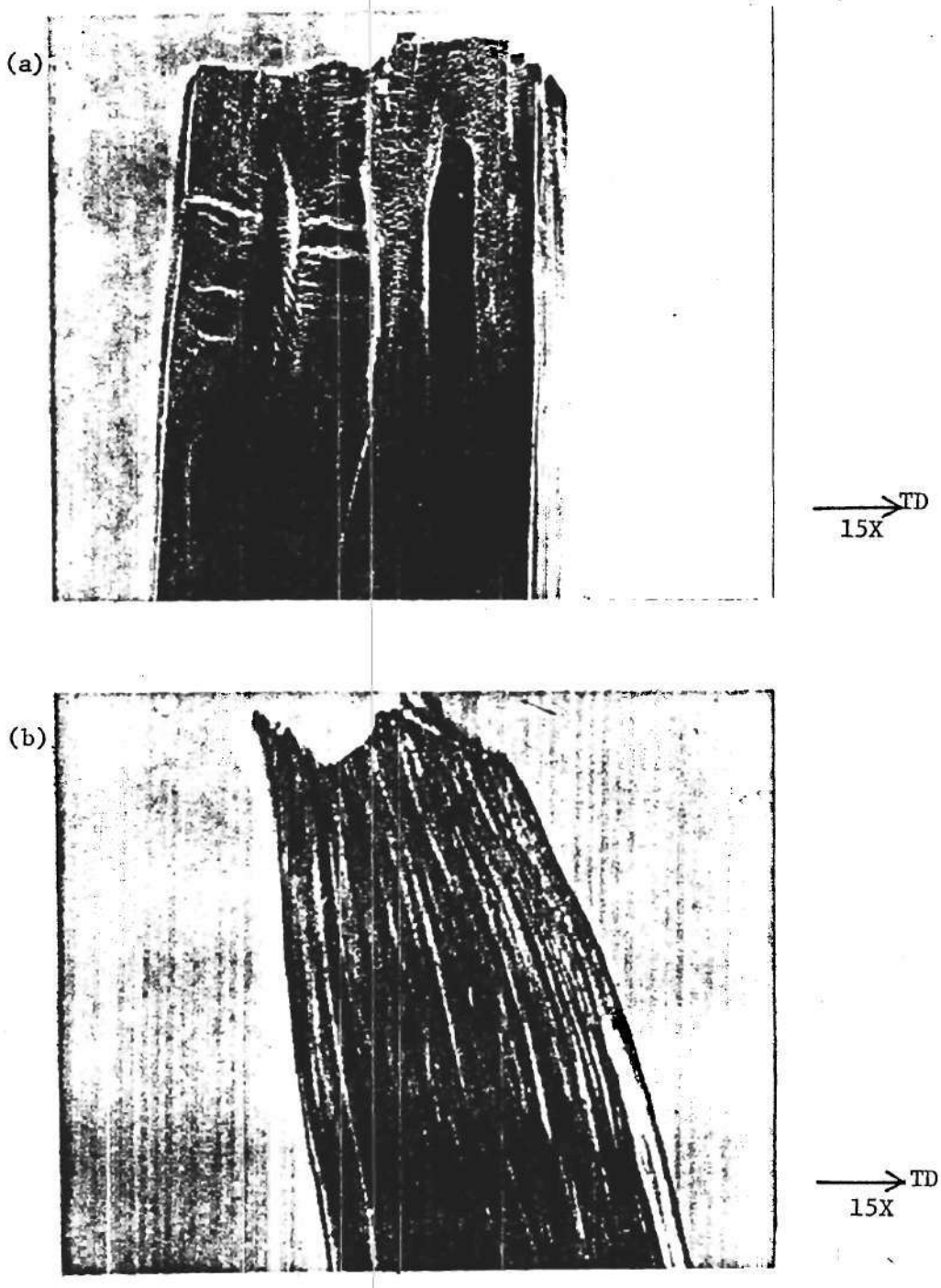

Figure 36. CY Alloy Furnace Cooled from 910°C, Tensile Specimen Tested at 350°C: (a) macrograph showing "orange peel" effect, and (b) "orange peel" effect and severe flow near fracture surface.

exhibiting deformation typical of both the CX and CY alloys in the furnace cooled and water quenched and aged conditions. The extensive necking which occurred near the fracture surface was observed only for the furnace cooled materials. An "orange peel" type effect can be seen in the prior β grains giving the surface relief evident in Figure 36a. This effect was found to some degree in all heat treatments. It tended to "wash out" more quickly with increasing distance from the fracture surface in the water quenched/aged materials. Figure 37 shows a typical area 2-3 mm away from the fracture surface. The "orange peel" effect noted above can still be observed, however to a much lesser degree. Some indication of coarse planar type slip bands is seen in this micrograph. This was observed in all alloys in regions where deformation was less severe.

TEM specimens were prepared from the gauge section of furnace cooled materials approximately 5-10 mm from the fracture surface since the highly deformed material near the fracture was not conducive to deformation structure observation. Figure 38 gives an example of the deformation structure in this area of the CX alloy furnace cooled from 910°C. Here it can be seen that the primary α grains are elongated and show very high dislocation densities and some tendency toward cell formation (Figure 38a). Figure 38b shows an area where small incoherent precipitates have pinned dislocations producing deformation free areas similar to small cells. This was observed in both the CX and CY type alloys. The deformation structure at a distance of 5-10 mm from the fracture surface consisted of homogeneous dislocation tangles of medium density. This structure was typical of

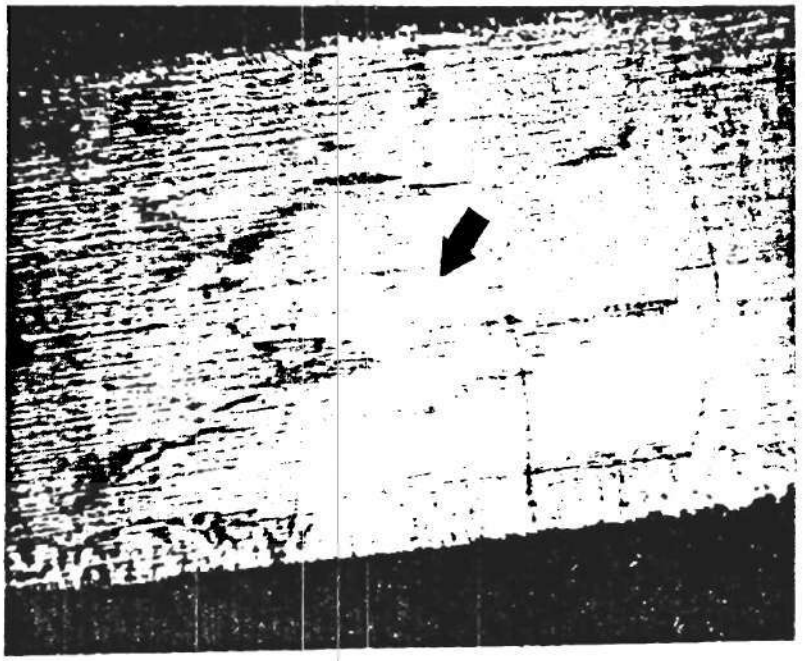

45X

Figure 37. CY Alloy Water Quenched from 910°C Aged 1 Hr. at 450°C. Shows a Typical Area 2-3mm from the Fracture Surface. The "Orange Peel" Effect plus Possible Slip Bands (Arrowed) are Evident.

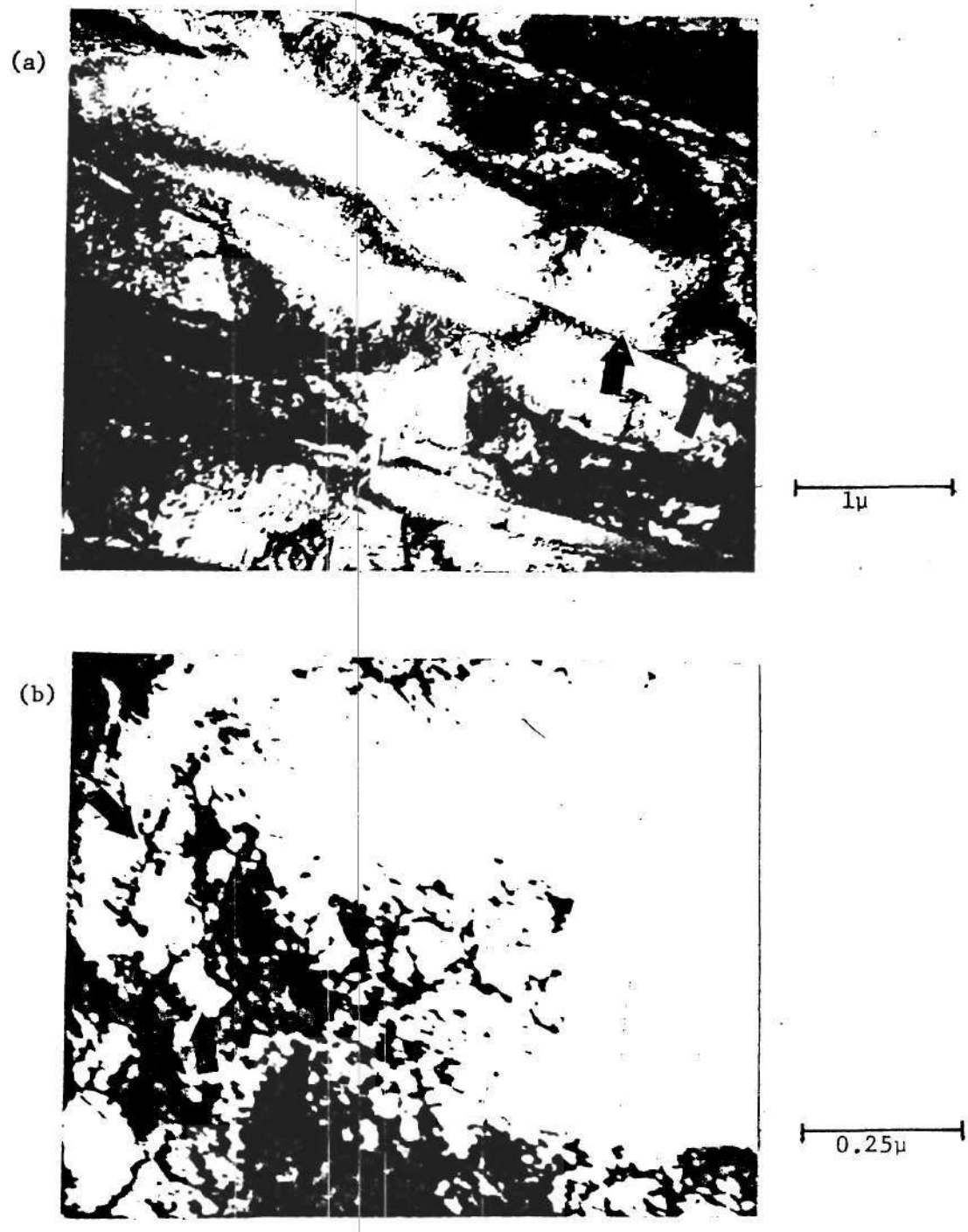

Figure 38. CX Alloy Furnace Cooled from 910°C: (a) severe deformation near the tensile specimen fracture surface and elongated cells, and (b) dislocation free "cell like" areas (arrowed).

the deformed CX and CY type materials in the furnace cooled condition (Figure 39). Both materials exhibited dislocation arrays consisting of long straight dislocations as shown in Figure 40. Figure 39, on the other hand, shows the precipitates to be effective barriers to dislocation motion and appear to be looped rather than sheared.

The deformation structure of the water quenched materials were more difficult to interpret and they differed somewhat for the CX and CY alloys. Figure 41 shows the typical deformed area in the CX type alloy. This shows a high density of dislocations with some tendency towards banding. This micrograph also shows the disruption of the twin interface by the dislocation structure, at point A. Figure 42 shows a twin which appears to have sheared slightly by the deformation structure at point A. In Figure 43 fine micro-twins can be seen in a larger twin at point A. The tendency towards banding noted in the CX alloy water quenched from 1000°C was not evident in the CY alloy. Figure 44 shows a typical deformed area in the CY alloy. Heavy dislocation structure is evident along with shearing of twins at A which was observed in the CX alloy. Figure 45 shows apparent antiphase domain boundaries which were very prominent for this material and heat treatment. These were not observed in the undeformed structure to any great extent. It appeared that in both the CX and CY alloy quenched/aged from 1000°C, the long straight plates had been broken up either by large twins or slip. Figure 46 shows two long grains which exhibit discontinuities at A -- this type of structure was typical in both alloys. In general, deformation in the 1000°C quenched/aged materials appeared to consist of homogeneously

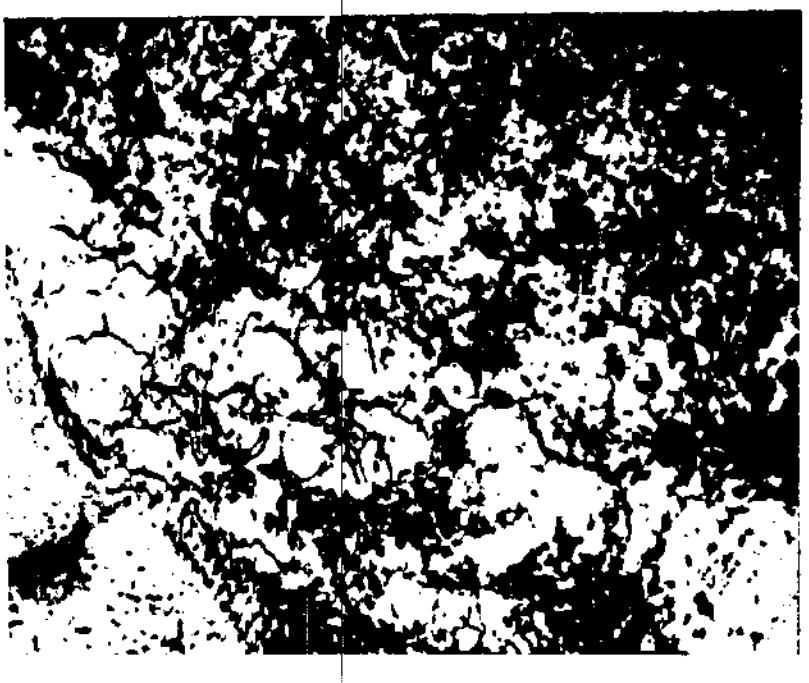

Figure 39. CX Alloy Furnace Cooled from 910°C, Deformed at 350°C. Typical Area 5-10mm from Fracture Surface.

Figure 40. CX Alloy Furnace Cooled from 910°C, Deformed at 350°C. Long Straight Dislocation Arrays.

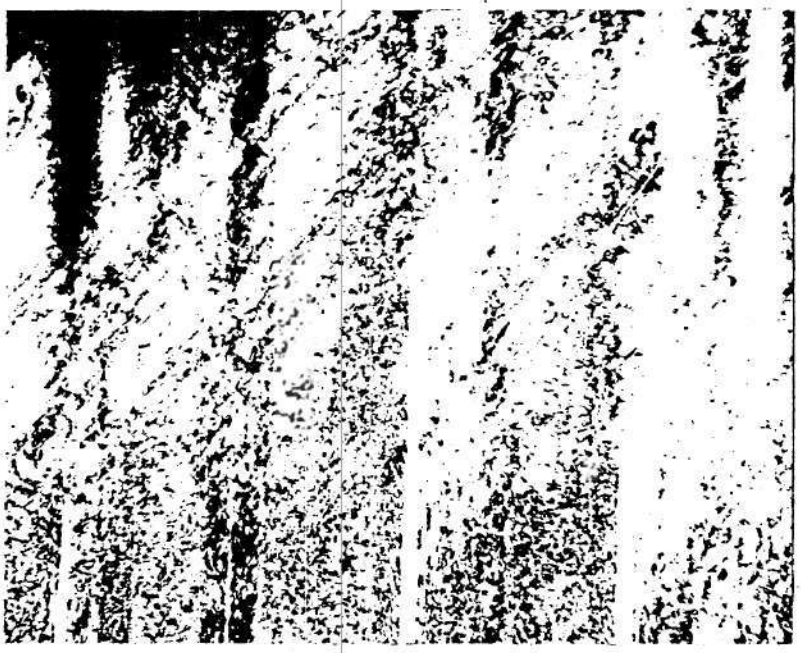

Figure 41. CX Alloy Water Quenched from 1000°C Aged 1 Hr. at 450°C, Deformed at 350°C. Typical Deformation Structure.

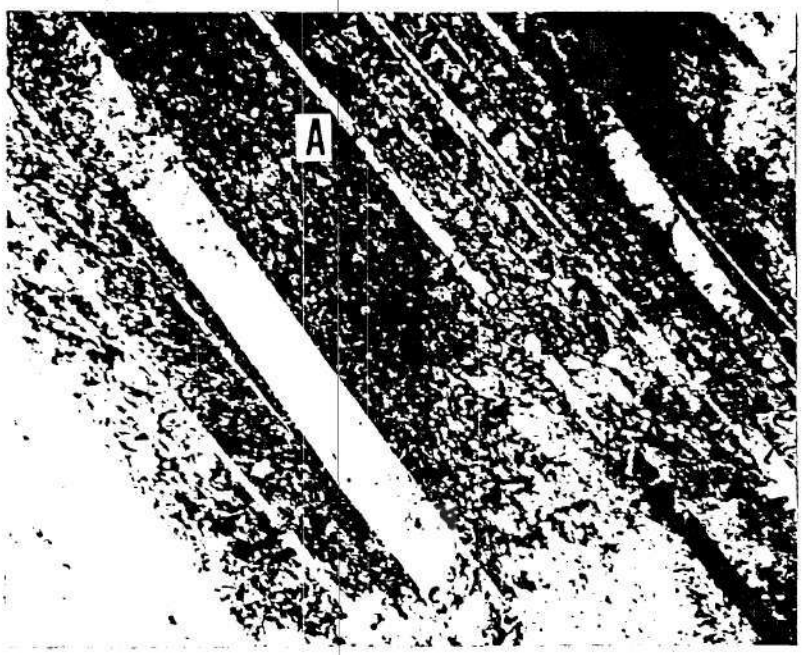

Figure 42. CX Alloy Water Quenched from 1000°C Aged 1 Hr. at 450°C, Deformed at 350°C. Twin Boundary Disruption at Point A.

Figure 43. CX Alloy Water Quenched from 1000°C Aged 1 Hr. at 450°C, Deformed at 350°C. Shows Fine Twins Within Larger Twinned Area.

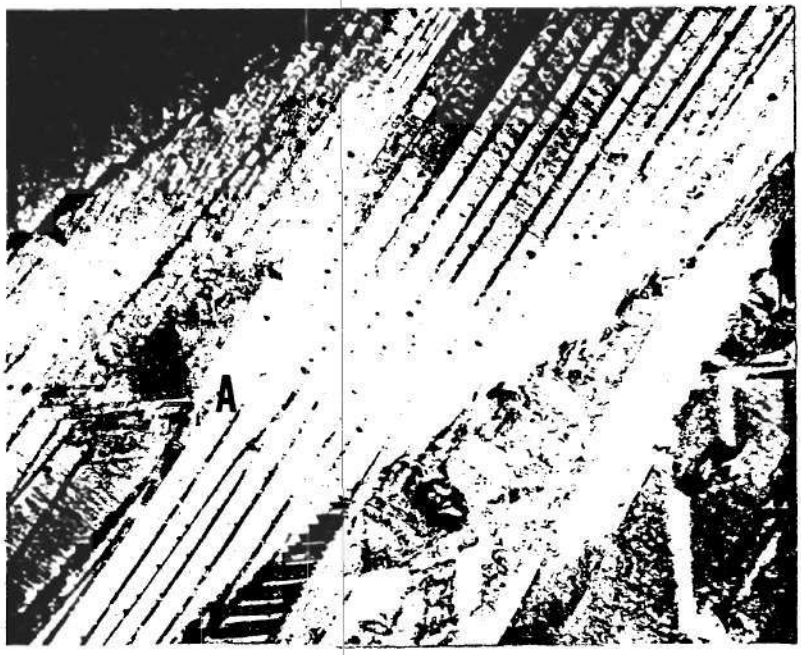

Figure 44. CY Alloy Water Quenched from 1000°C, Aged 1 Hr. at 450°C, Deformed at 350°C. Typical Deformed Area with Twin Boundary Disruption at A.

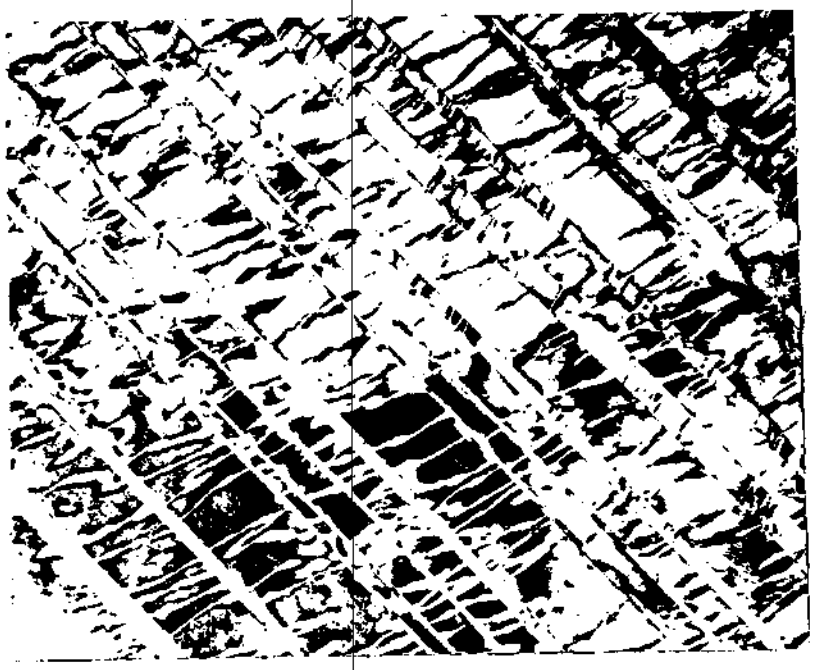

Figure 45. CY Alloy Water Quenched from 1000°C, Aged 1 Hr. at 450°C, Deformed at 350°. Shows Apparent Antiphase-Domain Boundaries.

Figure 46. CY Alloy Water Quenched from 1000°C, Aged 1 Hr. at 450°C, Deformed at 350°C. Discontinuities in Large α' Plates at A.

distributed dislocation tangles (Figure 41). Some evidence of microtwinning existed but was difficult to detect due to the large number of twins present in the as-heat-treated structure.

The materials water quenched/aged from 910^{o}C exhibited similar deformation structures. The relatively large equiaxed α grains showed dense homogeneous tangles with some indication of cell formation being noted (Figure 47). Many primary α grains exhibited structures similar to Figure 48, where relatively less dense dislocation networks can be seen. As in the furnace cooled alloys the precipitates appeared to be effective obstacles to dislocation motion. A typical area in deformed martensite plates is shown in Figure 49. This shows both the dislocation structure within the twinned platelets at A and the disruption of the twins. It can be seen that the twin interface will accomodate deformation in the form of slip to a certain level after which the twin interface coherency is disrupted. No tendency for cell formation was noted in the martensitic grains. Figure 50 shows apparent stacking faults prevalent in the CX material in the deformed condition.

Figure 47. CX Alloy Water Quenched from 910°C, Aged 1 Hr. at 450°C, Deformed at 350°C. Typical Deformation Structure in a Large Equiaxed Grain Showing Possible Cell Formation.

Figure 48. CY Alloy Water Quenched from 910°C, Aged 1 Hr. at 450°C, Deformed at 350°C. Typical Dislocation Network in a Large Primary α Grain.

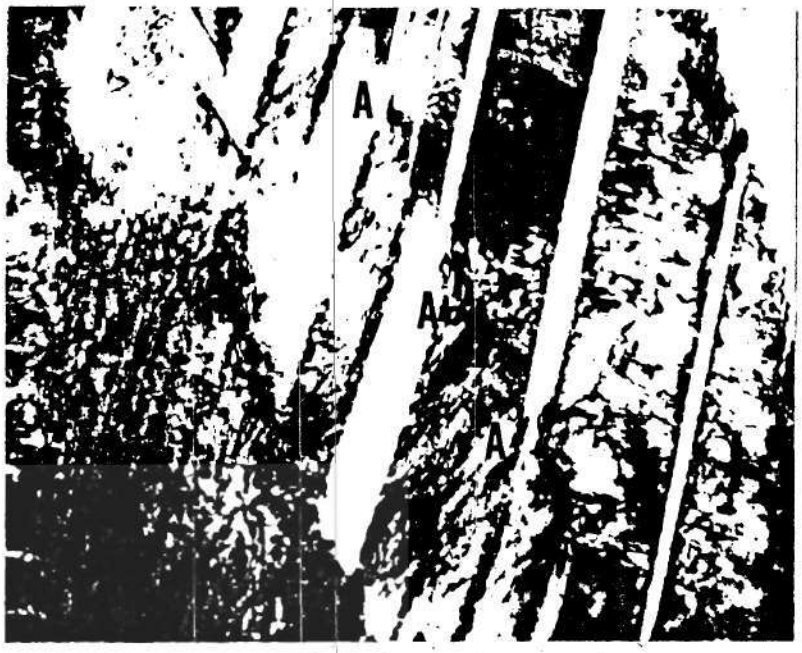

Figure 49. CY Alloy Water Quenched from 910°C, Aged 1 Hr. at 450°C, Deformed at 350°C. Typical Deformation Structure Showing Twin Interface Disruption at "A".

Figure 50. CX Alloy Water Quenched from 910°C, Aged 1 Hr. at 450°C, Deformed at 350°C. Possible Stacking Faults.

CHAPTER V

DISCUSSION OF RESULTS

Microstructure

The materials and heat treatments studied show the general characteristics of ($\alpha + \beta$) Zr and Ti alloys. They can be heat treated to give predominately a transformed β structure with a minor amount of primary α or by slower cooling an equilibrium α structure with small amounts of β or $\beta + \omega$.

The water quenched martensitic structures are in general the same for both the 1000°C and the 910°C water quench. The precipitation and growth of the primary α phase in the 910°C water quench accounts for the large difference in martensite plate size between this heat-treatment and the 1000°C quench/age. The formation of these relatively small particles during solutionizing in the $\alpha + \beta$ region restricted the growth of the martensite plates during the quench. Since the 1000°C solutionizing temperature is in the single phase β region no restrictions to martensite plate growth occurred and the martensite plates in many cases span an entire prior β grain. On a finer scale, however, the two quenching temperatures yielded similar structures. The finer martensite plates in the 1000°C quench were evidently formed after the large plates, and were subject to growth restrictions similar to the 910°C quench, hence the finer martensite plates are very similar in size. Both quenching temperatures exhibit the heavily

twinned martensite plates evident in other studies[47,4]. It has been noted that the addition of >0.6% Nb to Zr promotes the twinned martensite formation observed here[47]. In these materials the larger martensite plates were always heavily twinned whereas some smaller plates were not. This has been observed in the Zr-2.5 wt% Nb system and is attributed to the operation of a critical stress requirement for twin nucleation[47]. The slight difference in the amount of primary α present in CX and CY alloys water quenched from 910°C is thought to be due to the effect of the Al addition and will be discussed later.

The materials water quenched from 800°C showed, as expected, a large amount of primary α formed during solutionizing. The β transformation product, however, did not appear to be the expected martensitic phase. It is evident that the β phase which existed at the solutionizing temperature is greatly enriched in solute and this may effect the martensite transformation. This aspect was not studied in any detail and is still unclear.

The absolute volume fractions of β + ω obtained from quantitative x-ray diffractometry were not accurate due to the large amount of overlap between the β and ω peaks. The actual calculated value would be accurate only at low ω/β rations. However, the trend indicated appears to be valid. The sharp increase in the amount β + ω observed at 875-850°C for the CX alloy and 850°C-825°C for the CY alloy is consistent with the fact that there is a minimum concentration of solute for which β is stable at room temperature. This minimum concentration is 5 wt% Mo and 15 wt% Nb[10]. A similar behavior has

been observed in the case of ω formation at 3.2 wt% Mo and 7.5 wt% Nb[48,49]. As the solutionizing temperature is lowered the solute concentration of the β remaining is moved towards this minimum stabilizing concentration. The x-ray diffraction data of Table 6 clearly shows the presence of retained β in all samples except the 1000°C water quench and the CY alloy water quenched from 910°C. Because of the proximity of β and ω peaks the detection of ω by x-ray diffraction is difficult. However, as shown above, the occurence of retained β should be accompanied by the formation of ω at suitable quenching rates.

Two distinct types of ω have been observed in Zr alloys, a so called "metastable" ω formed on aging a quenched material containing retained β phase, and a diffuse ω formed athermally during quenching[10]. The metastable ω has been shown to be hexagonal with an axial ration of 6.22 ± 0.002 with no compositional variation, and lattice parameters of a_o = 5.02Å and c_o = 3.000Å[25]. Diffuse ω is reported to be hexagonal with an axial ration of 0.616 having lattice parameters which vary with solute concentration[10]. Williams, et al.[4] and Ibrahim, et al.[41] observed ω formation in the CX and CY alloy air cooled from the (α + β) region. Careful examination of the x-ray data of Tables 7 and 11 plus the x-ray scans themselves, clearly indicates the presence of ω in the materials quenched/aged from 800°C. In the materials quenched from 910°C and aged at 450°C the d = 1.33Å line can be attributed to the formation of β Nb since isothermal ω formation would not be expected. Aging the materials water quenched from 800°C produced a shift in the $\omega(11\bar{2}2)$ line possibly due to solute rejection by the supersaturated ω phase. The relationship between the

quenching temperature, α' martensite, retained β, and ω formation depends on the electron to atom ration.

As the quenching temperature is lowered in the α + β region α starts precipitating out of the β matrix. Because of the limited solubility of Nb and Mo in the α phase most of these solutes go to enrich the β phase. Therefore as the temperature is reduced in the (α + β) region we see an increase in the β Mo and Nb concentraion. It has been shown in Zr-X systems, X being any β stabilizing element, that the stabilization corresponds to a well defined electron to atom ratio[49]. At an e/a ratio of 4.06 or less, 100% α' is observed on quenching. At an e/a ration of 4.144, 100% β can be retained at room temperature on quenching. At a ratio between these two a mixture of α' + β + ω can be obtained on quenching depending on the M_s temperature. Luke, et al.[49] postulate the possible transformation products obtained on quenching in order of increasing β solute content as follows:

$$\beta \rightarrow \alpha' \tag{1}$$

$$\beta \rightarrow \alpha' + \omega + \beta \tag{2}$$

$$\beta \rightarrow \beta + \omega \tag{3}$$

$$\beta \rightarrow \beta \tag{4}$$

The apparent sharp increase in the amount of β + ω in the CX and CY alloys at 875°C and 850°C respectively would support this hypothesis.

The quenching temperature at which β + ω is first observed is the only major difference in the microstructure of the two alloys.

This cannot be explained in terms of amounts of β stabilizers present. From Table 5 it can be seen that although the CY alloy contains an additional amount of α stabilizer in the form of 1% Al, the total amount of α stabilizers present is less than the 3.5% Sn present in the CX alloy. However, it has been noted that Al has a pronounced effect on the β stability in both the Ti and Zr systems[32,33]. The addition of Al to the Zr-Mo system tended to stabilize the β against athermal ω formation[32]. Similarly, Crossley, et al.[50] noted that the addition of Al to β stabilized Ti alloys suppressed the formation of ω and retained β. This is possibly attributed to the increasing of the M_s temperature due to the Al addition. It is possible that the addition Al has suppressed the $\beta \rightarrow \beta + \omega$ or $\beta \rightarrow \omega$ transformation in the CY alloy relative to the CX. This could account for the offset in the quench temperatures at which $\beta + \omega$ is observed.

The lack of a twinned martensitic type structure in the 800°C water quenched/aged materials is not clearly understood. It has been noted that the tendency to form twinned or untwinned martensite is related to alloy content and plate volume[47]. With respect to plate volume Williams[47] noted that the tendency for inhomogeneous shear to be satisfied by twinning is proportional to plate volume. In the 800°C water quenched materials the presence of large amounts of primary α greatly restricted plate growth and could have a large effect on the type of martensite formed.

The furnace cooled materials represent an equilibrium structure as indicated by the similarity in the materials cooled from 800°C and

910°C. The presence of retained β has been confirmed by x-ray diffraction; however, no ω formation has been found. The amount of retained β as measured by quantitative x-ray diffractometry can account for only a small portion of the second or transformed phase. The location of the retained β in these alloys has not been studied in depth. Ibrahim, et al.[41] reported the presence of narrow stringers of retained β between the primary α grains in alloys furnace cooled from similar temperatures. In a Ti-6, Al-4, V treated similarly, the β phase was found to consist of narrow rim of the edge of the transformed β region[51]. It is reasonable to expect a similar structure in these materials considering the mechanism of formation. As these alloys are slowly cooled from the two phase region the β' phase transforms to α by diffusion controlled growth. The remaining β phase is progressively enriched in solute. At some temperature the β solute enrichment will reach the point where the β can be retained at room temperature. Since the entire process is diffusion controlled the region nearest the phase boundary should be most enriched in solute and will have the greatest probability of being retained at room temperature. Calculation of the lattice parameter of the β phase present in these alloys indicates significant solute enrichment has occurred. The calculated a_o was 3.56Å compared to 3.60Å for pure zirconium.

The distinct reciprocal lattice streaking observed in the transformed β region was thought to be due to the presence of many very fine precipitates. No attempt was made to identify these precipitates; however, Zr_4Sn, $ZrMo_2$ and β Nb precipitation has been

observed in these materials[41].

The alloys furnace cooled and water quenched from 800°C have mainly primary α precipitates at that temperature. This primary α has random orientation giving rise to the random textures of Figures 18, 20, 30, 32. The alloy quenched from 1000°C has α' platelets formed by the reaction α(R.T.) → β(1000°C) → α'(athermal). Since, perhaps, same crystallographic relationships exist between β phase and α and α' phases, the as-quenched alloy should have the same texture as the unheattreated rolling texture. However, the α' platelets are heavily twinned, perhaps on $(10\bar{1}2)$ planes. A $(10\bar{1}2)$ twin transformation of Zr rolling (1001) texture is schematically shown in Figure 51. This agrees to some extent with the texture of the 1000°C as-quenched alloys (Figures 16 and 19).

Mechanical Properties

All alloys and heat treatments showed similar aging response with the exception of the CY alloy water quenched from 1000°C. Apparently the Al addition effects the kinetics in these materials. Why this effect was not observed in the lower temperature quenches is unclear. It is possible that the increased number of precipitation sites in the form of grain boundaries in the finer grained materials accelerated the aging process in the 910°C water quench. The amount of solute in the α' decreases as the quenching temperature is lowered. This in turn inhibits the aging response due to less precipitation hardening. This effect can be observed in the lower response of the materials quenched from 910°C and 800°C. The CX alloy quenched

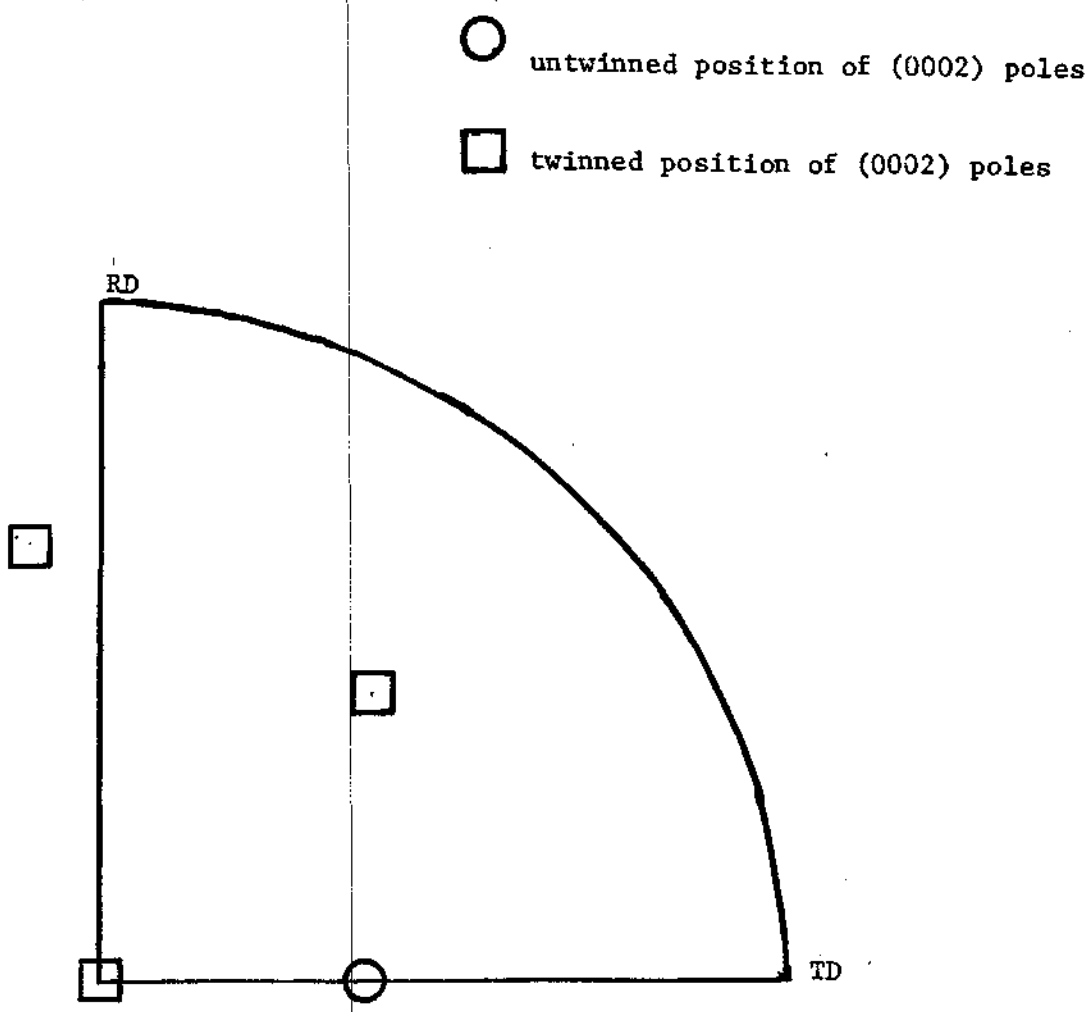

Figure 51. Position of (0002) Pole of as Rolled Zirconium Before and After $(10\bar{1}2)$ Twinning Transformation.

from 1000°C and aged 1 hour at 450°C shows approximately the same hardness as the 910°C water quench, however 1 hour aging is not the maximum hardness (Figures 42 and 43).

The CY alloy exhibits the highest strengths in both the furnace cooled and water quenched conditions. This has been attributed to the solution strengthening effect of the Al[4]. In the furnace cooled condition little change in strength with solutionizing temperature is observed indicating that this is an equilibrium structure.

Since the 910°C water quenched and aged materials contained approximately 0.20 volume fraction of the relatively weaker primary α it was expected that these would exhibit lower strengths than the 100% martensitic 100°C water quench. However, the 910°C quenched and aged materials were significantly stronger. The lower strength of the 1000°C water quench is apparently due to the larger grain size in this material. Also it has been noted that the 1000°C water quenched and aged materials exhibited a stronger texture than the 910°C quenched/aged material. This could possibly have an additional detrimental effect on the strength of 1000°C quenched/aged material. The hardness values do not exhibit this higher strength in the 910°C quench/aged materials. Hardness measurements are indicative of both the strength and work hardening tendency of a material and hence reflect to some degree the deformation systems operating. The difference in strengths between the 1000°C and 910°C quenched/aged is apparently offset by changes in the work hardening tendency. This would tend to indicate differences in the deformation system prevalent in the two materials. The hardness numbers for the CX and CY alloys in the

as-quenched condition for various quenching temperatures are shown in Table 13. These indicate the martensite volume fraction and plate size do not have a significant effect on the overall strength. Comparing the hardness changes observed with changes in quenching temperatures with those obtained on aging show the precipitation hardening to be the most potent strengthening effect.

Deformation

Macrographs of all materials showed the "orange peel" effect where prior β grains deformed as a unit. This indicates that colonies of α particles within the prior β grains are similarly oriented, as was indicated in the texture studies. Although the furnace cooled materials exhibited much less texture than did the water quenched materials, a corresponding difference in the relief effect was not noted. The low ductility of the water quenched materials caused this effect to "wash out" very quickly. From this "orange peel" effect it appears that the deformation is relatively homogeneous within a prior β grain due to similar grain orientation. Deformation in the furnace cooled materials consisted of dense homogeneous tangles with the beginnings of cell formation. This indicated that coarse slip is possible in these treatments.

Deformation in the water quenched materials was difficult to analyze but was in general similar to Zr-2.5 Nb studies[47]. In these materials the twin boundaries appeared to be somewhat effective as barriers to dislocations but were less so than high angle boundaries. E. Tenchoff[16] has shown that in rolled Zircaloy 2 exhibiting the

type texture observed in the CX and CY alloys tensile loading is accommodated by $(10\bar{1}0)$ $\langle 11\bar{2}0\rangle$ slip and $(11\bar{2}2)$ twinning. If the twins present are $(10\bar{1}1)$ type then a dislocation can only move without obstruction the full width of an α'' platelet on one set of prism planes. This would account for the significant disruption of the twin interfaces at higher deformations. This was true of both the 910°C and the 1000°C water quenched materials. No evidence of cell formation was noted in the α' martensite in either the 910°C or 1000°C quenched materials. In the 1000°C the larger grains were in many cases sheared as twinned. Why this was not observed in the 910°C quenched materials is not understood. The tendency towards banding in these materials can be related to the interaction between dislocations and the precipitates. If the precipitates present are coherent and can be sheared dislocation banding is possible. However, if the precipitates present are incoherent and looping is the method of interaction, then dislocation tangles will be prevalent. The existence of dislocation bands in the CX alloy and not in the CY could possibly be related to the existence of ordered phases in this alloy. A large number of antiphase domain boundaries were observed in the CY material. In the presence of an ordered structure dislocation motion tends to be more restricted since cross slip is not prevalent. However, no dislocation banding was noted in the CY material.

The large α grains in the 910°C water quenched generally exhibited a deformation structure similar to the furnace cooled materials. The cell formation seen here again indicates that cross slip is possible. The fact that no cell formation is seen in the α'

martensite can be attributed to the effect of solute content on the stacking fault energy. Mo and Sn have been shown to have a measurable effect on the stacking fault probability in zirconium[34].

CHAPTER VI

CONCLUSIONS

Two complex zirconium base alloys were studied in order to determine those microstructural features which affect the strength and deformation modes. Two widely different heat treatments were studied in detail. Several conclusions can be drawn.

1. These materials are readily heat treatable with widely varying structures and strengths obtainable. Minor alloy additions appear to have little affect on the $\beta/\alpha + \beta$ transus.
2. Materials exhibiting high strength and low ductility consisting primarily of α' martensite can be obtained by water quenching. These materials show a significant aging response. The furnace cooled materials exhibit relatively low strength and high ductility, and show no aging response.
3. The addition of Al appears to have affected several areas. In general, the CY materials which contained Al were stronger than the corresponding CX alloy in all heat treatments. This is thought to be due to solution hardening. The Al containing materials showed a greater response to aging and in some cases the aging kinetics appeared to be altered by the Al addition. In addition, the Al appears to inhibit the ω formation during quenching.
4. The texture exhibited by these materials was typical of rolled Zircaloys. A $(110)\beta/(0002)\alpha$ Burgers relationship was indicated for

the isothermally formed primary α. However, the α' martensite appeared to form on a particular habit plane giving a characteristically sharp rolling type texture. When the structure consisted of both primary α and α' martensite the texture was not as sharp and appeared to be a superposition of the α' texture and the β texture.

5. The strengths of these materials appear to be related to several factors. As was mentioned Al is a potent strengthener. The α' martensite plate size has a significant effect on the elevated temperature tensile strength. The presence of small amounts of primary α in the martensitic matrix actually strengthened these materials since it inhibited α' plate growth. Precipitation hardening is the most potent strengthener present.
6. The hardness of these alloys varies little with quenching temperatures in the 1000°C to 800°C range. This has been attributed to differences in the work hardening rate for the different treatments.
7. In all materials the "orange peel" deformation structure showed the high angle prior β grain boundaries to be more effective barriers to dislocation motion than the low angle boundaries. The deformation modes prevalent for the CX and CY alloys in the furnace cooled condition were similar consisting of dense homogeneous tangles. The precipitates present also appear to be effective barriers to dislocation motion. The deformation structures in water quenched materials were difficult to interpret, but showed some differences. Both dislocation tangles and bands

were noted in the CX alloy while the CY alloy showed only tangles. This has been associated with the type precipitates present in the two materials. The deformation structure in the primary α grains in the α' martensite matrix was similar to the furnace cooled materials.

APPENDIX I

Specimen Preparation for Optical Microscopy

1) Grind to 600 grit SiC.

2) Touch up on 6μ diamond.

3) Touch up on 1μ diamond.

4) Polish on 1 Al_2O_3 slurry using a small amount of a fresh solution of 250 ml H_2O, 22 ml HNO_3, and 3 ml HF. Polish for approximately 15 sec on a nylon cloth.

5) Repeat step 4 for 0.3μ Al_2O_3.

6) Repeat step 4 for 0.05μ Al_2O_3 on a micro-cloth.

7) Anodize in Pickelsimer's Solution at 115 volts with stirring:

60 ml absolute ethanol
35 ml distilled water
20 ml glycerin
10 ml Lactic Acid
5 ml Phosphoric Acid
2 gm Citric Acid

APPENDIX II

Program for Volume Fraction Determination

```
00100       PROGRAM MAIN(INT,CON,OUTPUT,TAPE4=INT,TAPE5=CON,TAPE6=OUTPUT)
00105       REAL MULT(2,30)
00110       DIMENSION THE(2),VOL(2),RA(30),RB(30),EA(30),EB(30),EO(30)
00120       DIMENSION SPOT(2,30),EAO(3,30),EBO(3,30),Q(30)
00125       DIMENSION DIVB(30)
00130       DIMENSION FSQ(2,30),AANG(3),BANG(3),ATWT(2),COE(2),DIVA(30)
00135       REWIND4
00140       REWIND5
00150       THE(2)=212
00160       VOL(1)=1.86*1.0E22
00170       VOL(2)=2.2*1.0E22
00180       THE(1)=260
00190       READ(4,1000) NA,NB,NO
00200       DO 1 I=1,NA
00210     1 READ(5,8000) MULT(1,I),FSQ(1,I)
00220       DO 2 I=1,NB
00230     2 READ(5,8000) MULT(2,I),FSQ(2,I)
00240       COE(1)=5.5*1.0E-6
00245       COE(2)=5.5*1.0E-6
00250       RT=298
00260       TWOTM=.393
00270       WAVEL=1.5405
00280       ATWT(1)=91.22
00285       ATWT(2)=91.22
00290       N=NA
00300       DO 20 J=1,2
00310       PB=(1+((COS(2*TWOTM))**2))
00320       PART1=1+(((3/2)*COE(J)*2)*RT)
00330       PART2=1+0.026*(THE(J)/RT)**2
00340       PART3=(22973*RT)/(ATWT(J)*THE(J)**2)
00350       DO 10 I=1,N
00360       READ(4,2000) ANGLE
00370       SPOT(J,I)=ANGLE
00380       PT=(1+((COS(2*TWOTM))**2)*((COS(2*ANGLE))**2))
00390       P=PT/PB
00400       TFAC=1/(COS(ANGLE)*(SIN(ANGLE))**2)
00410       PART4=(SIN(ANGLE)/WAVEL)**2
00420       TWODEE=PART1*PART2*PART3*PART4
00430       Q(I)=MULT(J,I)*(VOL(J)**2)*FSQ(J,I)*EXP(-TWODEE)*TFAC*P
00440       IF(J.EQ.1) RA(I)=Q(I)
00450       IF(J.EQ.2) RB(I)=Q(I)
00460    10 CONTINUE
00470       N=NB
00480    20 CONTINUE
00490       WRITE(6,3000) (RA(I),I=1,NA)
00500       WRITE(6,4000) (RB(I),I=1,NB)
00510       READ(4,5000) (EA(I),I=1,NA)
00520       READ(4,5000) (EB(I),I=1,NB)
00530       WRITE(6,6000) (EA(I),I=1,NA)
00540       WRITE(6,7000) (EB(I),I=1,NB)
00550       READ(4,5000) (EO(I),I=1,NO)
00560       DO 40 J=1,NO
00565       DO 40 K=1,3
00570       READ(4,8000) AANG(K),BANG(K)
00580       DO 30 I=1,NA
00590       IF(AANG(K).EQ.SPOT(1,I)) EAO(K,J)=RA(I)
00600    30 CONTINUE
00610       DO 35 I=1,NB
00620       IF(BANG(K).EQ.SPOT(2,I)) EBO(K,J)=RB(I)
00630    35 CONTINUE
00640    40 CONTINUE
00650       AD1=0.0
```

```
00660       DO 50 I=1,NA
00670    50 A01=A01+EA(I)/RA(I)
00680       AO=A01/NA-NO
00690       B01=0.0
00700       DO 60 I=1,NB
00710    60 B01=B01+EB(I)/RB(I)
00720       BO=B01/NB-NO
00730       IF(NO.NE.0) GO TO 70
00740       A=AO
00750       B=BO
00760       GO TO 120
00770    70 B1=BO
00780       A1=AO
00790    80 AO=A1
00795       BO=B1
00800       SUM=0.0
00810       DO 90 I=1,NO
00813       DIVA(I)=EAO(1,I)+EAO(2,I)+EAO(3,I)
00816       DIVB(I)=EBO(1,I)+EBO(2,I)+EBO(3,I)
00820    90 SUM=SUM+(AO*EO(I))/(AO*DIVA(I)+BO*DIVB(I))
00830       A1=(A01+SUM)/(NA+NO)
00850       B1=BO
00870       SUN=0.0
00880       DO 110 I=1,NO
00890   110 SUN=SUN+(BO*EO(I))/(AO*DIVA(I)+BO*DIVB(I))
00900       B1=(B01+SUN)/(NB+NO)
00910       IF(ABS(A1-AO).GT.ERS.OR.ABS(BO-B1).GT.ERS) GO TO 80
00920       A=A1
00930       B=B1
00940   120 VA=A/(A+B)
00950       VB=B/(A+B)
00960       WRITE(6,9000) VA
00970       WRITE(6,9500) VB
00980  1000 FORMAT(6X,3I2)
00990  2000 FORMAT(6X,F6.3)
01000  3000 FORMAT(*INTENSITY FOR PURE ALPHA*/,8(4X,E11.4)/)
01010  4000 FORMAT(*INTENSITY FOR PURE BETA*/,8(4X,E11.4)/)
01020  5000 FORMAT(6X,F7.3)
01030  6000 FORMAT(*INTENSITY FOR OBSERVED ALPHA*/,8(6X,F9.3)/)
01040  7000 FORMAT(*INTENSITY FOR OBSERVED BETA*/,8(6X,F9.3)/)
01050  8000 FORMAT(6X,2F8.3)
01060  9000 FORMAT(*THE VOLUME FRACTION OF ALPHA IS*,F6.3/)
01070  9500 FORMAT(*THE VOLUME FRACTION OF BETA IS*,F6.3)
01080       END
```

BIBLIOGRAPHY

1. N. R. McDonald: Journal of the Australian Institute of Metals, 1971, vol. 16, No. 4, p. 179.

2. E. Smith: "Plastic Flow Concentration and Its Effect on Failure of Zircaloy Fuel Rod Cladding," Research Project 217-1, Failure Analysis Associates, Palo Alto, Calif., Sept. 1975.

3. C. D. Williams: Reactor Technology, 1970, vol. 13, p. 147.

4. C. D. Williams, C. E. Ells, and P. R. Dixon: Canadian Metallurgical Quarterly, 1972, vol. 11, No. 1, p. 257.

5. A. Garlick: Journal of Nuclear Materials, 173-74, vol. 49, p. 209.

6. C. C. Busby, R. P. Tucker, and J. E. McCauley: Journal of Nuclear Materials, 1975, vol. 55, p. 64.

7. J. C. Wood: Journal of Nuclear Materials, 1972-73, vol. 45, p. 105.

8. A. Garlick and P. D. Wolfenden: Journal of Nuclear Materials, 1971, vol. 41, p. 274.

9. M. S. Wechsler: Zirconium, 2nd ed., ed. G. L. Miller, Buttersworth, London, 1957.

10. D. L. Douglass: The Metallurgy of Zirconium, International Atomic Energy Agency, Vienna, Austria, 1971.

11. T. Anderson: Scandinavian Journal of Metallurgy, 1973, vol. 2, p. 251.

13. B. S. Hichman: Journal of Materials Science, 1969, vol. 4, p. 554.

14. P. G. Partidge: Metallurgical Reviews, 1967, vol. 12, p. 169.

15. R. E. Reed-Hill: Deformation Twinning, Proceedings, ed. R. E. Reed-Hill, J. P. Girth, and H. C. Rogers, Gordon and Breuch, New York, 1965.

16. E. Tenchoff: Zirconium in Nuclear Applications, ASTM Special Technical Publication, No. 551, 1974, p. 179.

17. J. L. Martin and R. E. Reed-Hill: Transactions of the Metallurgical Society of AIME, 1964, vol. 230, p. 780.

18. J. A. Jensen and W. A. Backofen: Canadian Metallurgical Quarterly, 1972, vol. 11, No. 1, p. 39.

19. O. M. Katz: "Some Observations on Zirconium and Its Alloys by Transmission Electron Microscopy," Paper Presented to The Electrom Microscopy Society Annual Meeting, New York City, August 1965.

20. E. N. Aqua and C. M. Owens: Transactions of the Metallurgical Society of AIME, 1967, vol. 239, p. 155.

21. J. E. Bailey: Journal of Nuclear Materials, 1962, vol. 7, No.3, p. 300.

22. R. F. Domagalo, D. W. Levinson, and D. J. McPherson: Journal of Metals, 1957, Oct., p. 1191.

23. H. A. Robinson, J. R. Doig, M. W. Mote, and P. D. Frost: Transactions of AIME, 1959, vol. 215, p. 237.

24. D. H. Sastry, M. J. Luton, and J. J. Jonas: Philosophical Magazine, 1974, vol. 30, p. 1187.

25. S. A. Aldridge and B. A. Cheadle: Journal of Nuclear Materials, 1972, vol. 42, p. 32.

26. G. P. Sabal: Journal of Nuclear Materials, 1970, vol. 34, p. 142.

27. B. A. Cheadle, C. E. Ells, and J. Van der Kuur: Zirconium in Nuclear Applications, ASTM Special Technical Publication, No. 551, 1974, p. 370.

28. E. M. Schulsom: Journal of Nuclear Materials, 1975, vol. 56, p. 38.

29. E. M. Schulsom: Journal of Nuclear Materials, 1974, vol. 50, p. 127.

30. L. M. Howe, M. Rainville, and E. M. Schulsom: Journal of Nuclear Materials, 1974, vol. 50, p. 139.

31. J. F. R. Ambler, E. M. Schulsom, and G. P. Kiely: Journal of Nuclear Materials, 1974, vol. 50, p. 107.

32. D. O. Northwood and J. Rezek: Journal of Nuclear Materials, 1972, vol. 42, p. 227.

33. G. A. Delvecchio, D. O. Northwood, and J. Rezek: Journal of Nuclear Materials, 1970, vol. 35, p. 67.

34. D. H. Sastry, M. J. Luton, and J. J. Jonas: Philosophical Magazine, 1974, vol. 30, p. 115.

35. D. J. Abson and J. J. Jonas: Journal of Nuclear Materials, 1972, vol. 42, p. 73.

36. D. O. Northwood: "Correlation of Alloy Microstructures and Properties," Atomic Energy of Canada Limited Report AECL-4159, 1970.

37. W. M. Rumball: Journal of the Less Common Metals, 1974, vol. 38, p. 237.

38. M. R. Warren and J. A. Itterhus: Canadian Metallurgical Quarterly, 1974, vol. 11, No. 1, p. 249.

39. W. M. Rumball and C. E. Coleman: Journal of Nuclear Materials, 1970, vol. 36, p. 147.

40. L. Kumar and R. Krishnan: Transactions of the Japanese Institute of Metals, 1972, vol. 13, p. 18.

41. E. F. Ibrahim, E. G. Price, and A. G. Wysiekierski: Canadian Metallurgical Quarterly, 1972, vol. 11, No. 1, p. 273.

42. C. E. Ells, I. Aitshincon, V. Fidleris, and W. J. Langford: "The Irradiation Response of a Group of Complex Zirconium Alloys," Proceedings of the Conference on the Irradiation Embrittlement in Fuel Cladding and Core Components, British Nuclear Energy Society, 1972, p. 43.

43. C. E. Ells and B. A. Cheadle: "New Zirconium Alloys for Pressure Tubes," Paper Presented at Japan-Italy-Canada Exchange Meeting, June, 1973.

44. E. E. Underwood: Quantitative Stereology, Addison-Wesley Publ. Co., Reading, Mass., 1970, p. 5, 25.

45. ASTM Standards, Part 31, E8-66.

46. A. F. Giamei and E. J. Freise: Transactions of the Metallurgical Society of AIME, 1967, vol. 239, p. 1676.

47. C. D. Williams and R. W. Gilbert: Transactions of the Japanese Institute of Metals, 1968, vol. 9, supplement, p. 625.

48. J. Winton and R. A. Murgatroyd: Electric Chemical Society, 1966, vol. 4, No. 7-8, p. 358.

49. C. A. Luke, R. Taggart, and D. H. Polonis: Transactions of the American Society of Metals, 1964, vol. 57, p. 142.

50. R. L. Blorn, R. W. Lindberg, and R. A. Lewis: 2nd International Conference on Titanium, Cambridge, Mass., 1972.

51. J. C. Chesnutt, J. D. Frandsen, A. W. Thompson, and J. C. Williams: "Influence of Metallurgical Factors on Fatigue Crack Growth in Alpha-Beta Titanium Alloys," Interim Report for Oct. 1, 1974 to Dec. 1, 1974, Contract Number F33615-74-C-5067 Project Number 7351, United States Air Force Systems Command 4950th Test Wing/PMRA Wright Patterson AFB, Ohio.